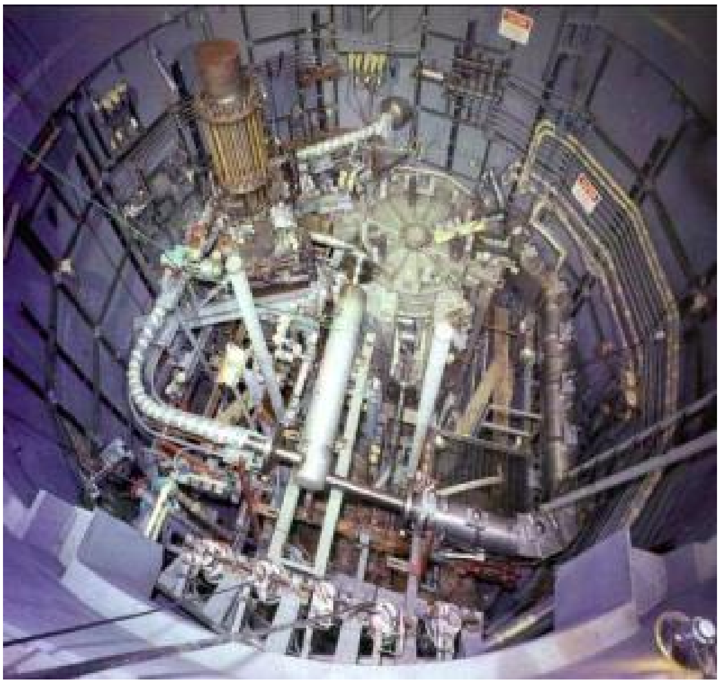

Computational Modeling of the Flow Field in a Molten Salt Reactor Core

Andreas van Wijk

Supervisor: Danny Lathouwers
Bachelor Thesis
Physics of Nuclear Reactors
Delft University of Technology
Delft, June 22, 2008

Abstract

The flow field in a molten salt reactor core was modeled using simplified equations. From these equations a computationally inexpensive computer code has been developed which is able to, amongst others, estimate the axial velocity distribution in the core and can be implemented in future or existing more elaborate codes to gain further insight into the behavior of the molten salt reactor, in particular the effects that a non-uniform axial velocity distribution might have on the heat exchange properties and flux profile in the reactor core. Several benchmark checks were performed to verify the validity of the model and code and calculations of the flow field in the 'Molten Salt reactor experiment' [10] setup were done at different flow rates of the fuel salt. A transient was also simulated. Calculations pointed out that axial velocities in the reactor core may vary as much as 30% and that during the start up of the MSRE setup the shape of the axial velocity profile changes with time.

Contents

Chapter 1

The Molten Salt Reactor

1.1 Introduction

Worldwide energy consumption has been the subject of intense discussion over the last few decades. It has become ever more apparent that fulfilling worldwide energy requirements using only traditional production methods will soon become impossible. Fossil fuels like coal and oil are fast running out and upcoming economies are putting an ever greater strain on the already decreasing resources.

Nuclear energy has always been a major contender in the quest for finding an alternative energy resource for the near future. Recent developments like the growing concern about global warming and the slow progress of solar and wind energy technology and production have sparked renewed interest in nuclear energy as a viable alternative to traditional production methods. China, India and Finland to name a few are already in the process of building new nuclear sites and other nations also show increased interest.

Safety issues however have always been a major concern in the nuclear power industry. Especially after the Czernobyl incident it became clear that if nuclear energy is going to play a major role in fulfilling our requirements, it has to be done in an inherently safe and environmentally friendly way.

One can distinguish between four generations of nuclear reactors, displayed in Fig. 1.1. The generation IV reactors are a set of theoretical reactor designs currently being studied around the world. Most of these designs are generally not expected to be available for commercial construction before 2030. The primary goals of generation IV reactors, with respect to the generation II and III type reactors currently in operation, are to improve nuclear safety, improve proliferation resistance, minimize waste and maximize natural resource utilization, and

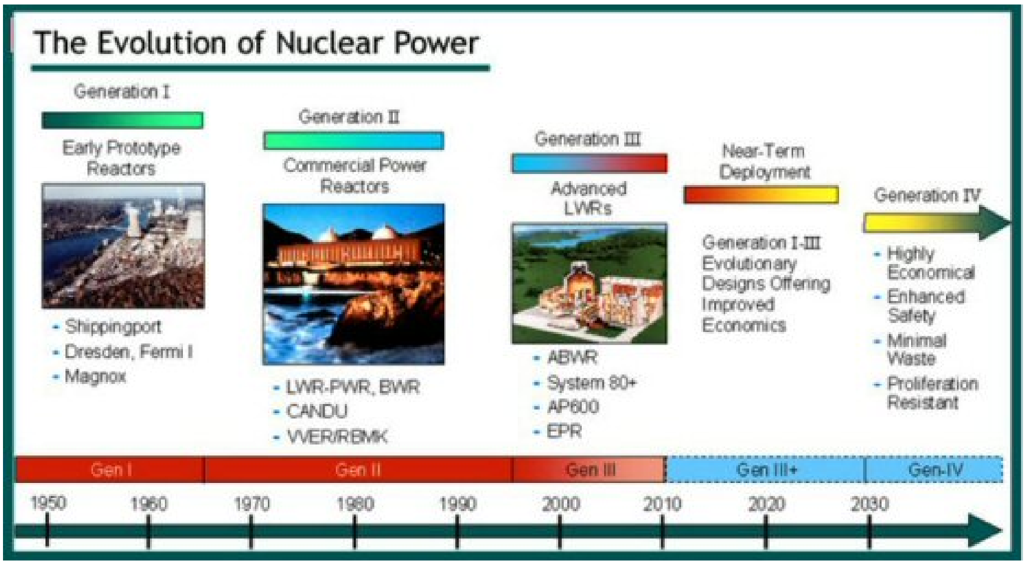

Figure 1.1: Overview of the different generations of nuclear reactors. Most nuclear reactors in operation today are part of generation II and III. The theoretical designs of generation IV are currently undergoing intense research.

to decrease the cost to build and run such plants.

A Molten Salt Reactor is a type of nuclear reactor in which the primary coolant is a molten salt. In many designs the fissile material is dissolved in the coolant salt and therefore moves through the reactor core during operation. Other MSR designs may rely on ceramic fuel dispersed in a graphite matrix with the molten salt providing high temperature low pressure cooling.

Generally speaking, molten salt reactors are an immature technology. So far only one, non-commercial, MSR has been built: the Molten Salt Reactor Experiment* (MSRE) of the Oak Ridge National Laboratory. It operated at full power for 1.5 years in the 1960's. The research done in the MSRE has led to almost all available experimental data, a summary of which can be found in [10]. The remainder of this thesis will therefore focus on the setup of the MSRE and the data associated with that setup. In the case of the MSRE the fissile material UF_4 (Uranium Tetra Fluoride) is dissolved in the coolant salt as $LiF - BeF_2 - ZrF_4 - UF_4$. In operating any nuclear power plant, the so called delayed neutron concentration is of crucial importance [6]†. After a fission event the resulting fission products may in some situations decay after some time, thereby possibly releasing a neutron which in turn will be able to induce fission in a fissile isotope. Since the fuel

---

[*] There have been other experiments which were focused on making a small MSR for airplane propulsion, but none of the scale of the MSRE

[†] Although the delayed neutrons make up only about 0.7% of the total amount of neutrons in a reactor core, it is by the grace of these delayed neutrons that one is able to run a nuclear power plant.

is not stationary, in many MSR designs one has to account for loss of delayed neutrons from the reactor core by convective transport, making the MSR rather exotic and hard to model correctly. Fig. 1.2 shows the reactor core of the MRSE setup in some detail. A full description of the geometry, fuel composition and other relevant parameters can be found in [10].

The Molten Salt Reactor (MSR), subject of this thesis, is included in the generation four set because it potentially has some advantages over other reactors:
The MSR closes the fuel cycle and potentially eliminates the need for both fuel enrichment and fuel fabrication.
Molten salt reactors can potentially be run at extremely high temperatures, such as those proposed for hydrogen production facilities. Higher temperatures also give better efficiency in electricity generation.
Molten Salts are good at trapping fission products and are mostly non-reactive in air. Even in the unlikely case of an accident, most radioactive fission products would stay in the salt in stead of being dispersed into the atmosphere. An already molten core is of course meltdown-proof.
The MSR has far better neutron economy and, depending on the design, a harder neutron spectrum. This makes it far less demanding on the quality of the fuel, allowing all three major nuclear fuels to be used: Uranium-235, Plutonium-239 and Uranium-233 (obtained by breeding from Thorium-232). It also allows for burning of transuranic wastes.

1.2 Aims and overview of this report

1.2.1 Aims of the report

This report deals with finding a simplified model describing the flow of coolant salt through the reactor core of a Molten Salt Reactor. Most studies done so far, like [4] and [1], use a single axial velocity for the fuel salt in the reactor core. In this research, the emphasis lies on finding an axial velocity distribution which may give new insights into the behavior of the MSR. A non-uniform distribution will, for example, have an effect on the heat exchange in the core which in turn will influence the neutron flux profile. A non-uniform distribution will also directly influence the neutron flux because precursors will have different residence times depending on the fuel channel in which they are created.
Due to the non-linear nature of the equations describing fluid flow and the fact that the reactor vessel has a complicated geometry calculations will quickly become involved. Simplified equations describing the flow are therefore presented, resulting in a computationally inexpensive computer code. The numerical results of this code may be used as input for future neutronics and thermo-hydraulics calculations.

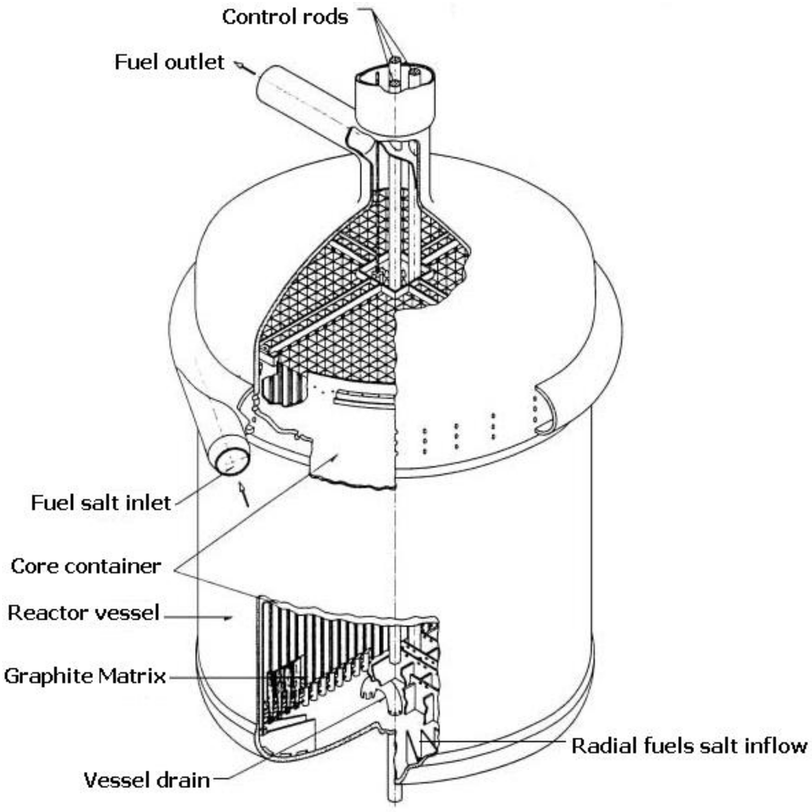

Figure 1.2: Overview of the core structure of the MSRE. The coolant salt enters from the sides of the lower dividing plenum and flows radially inward. Upon flowing inward, salt is discharged into vertical passages machined into the graphite matrix. The salt combines in the upper combining plenum and exits through the central fuel outlet header.

1.2.2 Overview

In chapter 2 some more attention will be given to the geometry of the MSRE. Starting from general fluid flow equations the simplified equations describing the flow field will be derived. Chapter 3 will deal with the discretization of the equations and the solution procedures will be outlined. In chapter 4 some benchmark checks will be performed to test the validity of the model and code. In chapter 5 the computational results obtained by the code are presented and some thought will be given to the validity of the code. Chapter 6 will provide conclusions and some further recommendations.

Chapter 2

Simplified model equations

2.1 Introduction

In this chapter simplified equations describing the flow field will be derived. First the geometry of the core structure of the MSRE will be treated in some more detail and three zones of interest will be identified. Starting from general fluid flow equations and using some simplifications and assumptions, the equations for the remainder of this thesis will be presented and applied to the zones of special interest.

2.2 Geometry description

The core structure of the MSRE consists of a cylindrical reactor vessel containing a graphite interior. The fuel salt flows from bottom to top through channels machined out in the graphite matrix, Fig. 2.1. Fuel salt entering the lower dividing plenum will distribute itself over the vertical channels, recombines in the upper combining plenum and exits through the outlet header. Three zones of interest are specified in Fig. 2.2:

Zone 1 represents the lower dividing plenum. The salt flows radially inward from the outside, losing radial momentum due to wall friction and turning at the channel heads while distributing over the vertical channels. The plenums are treated as straight cylinders, thereby neglecting the dome shape or curvature at the top and bottom of the cylinder in the actual assembly. This sacrifice is made in order to keep the geometry simple.

Zone 2 represents the graphite matrix which houses most of the fuel salt. In zone 2 the actual fission takes place and it is the zone where most heat is generated. The channel entrances, Fig. 2.3, are regularly spaced and distributed over the

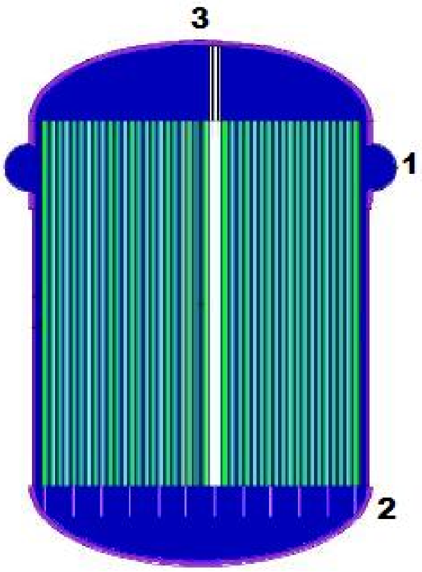

Figure 2.1: Schematic of the MSR reactor vessel. The fuel salt enters from the sides at 1, is guided down along the outer wall to 2 where it enters the lower dividing plenum. The salt makes its way up through channels machined out in the graphite matrix and combines in the upper combining plenum to exit at 3.

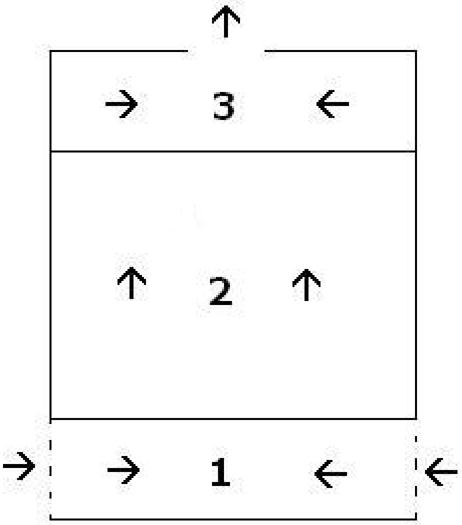

Figure 2.2: Schematic of the core structure as proposed by the author. Three zones are marked by the numbers one to three. Zone 1 represents the lower dividing plenum, zone 2 the reactor core and zone 3 the upper combining plenum. The arrows indicate the direction of the flow.

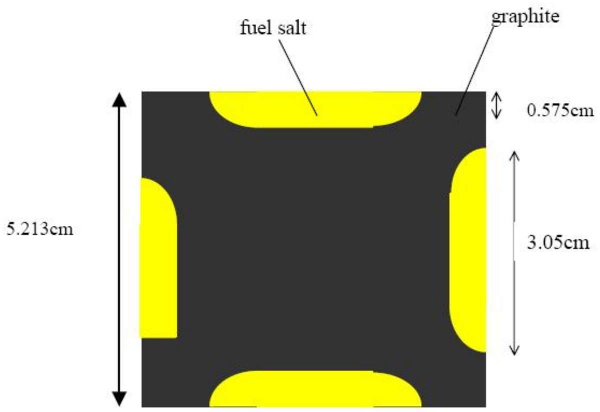

Figure 2.3: Schematic of the channel heads machined out in the graphite matrix of the MSRE.

top of the entire lower plenum. Because there are so many channel heads and they are regularly spaced it is more convenient to represent the graphite matrix as a uniformly porous medium. Making this assumption results in a rather big simplification of reality. Details of the flow field around channel entrances are completely discarded in favor of computational and analytical simplicity. In [2] and [9] it is shown that treating a manifold with a large number of uniformly spaced branch points as a uniformly porous medium gives an accurate description and is favorable above a discrete branch point description. The dimensionless porosity is defined as:

$$\alpha = \frac{\text{total entrance area of channel heads}}{\text{total area of top of lower plenum}} \tag{2.1}$$

Alternatively, from Fig. 2.3: the yellow area divided by the black and yellow area.

Zone 3 represents the upper combining plenum which is in essence similar to the lower dividing plenum 1, except that the salt enters from zone 2 and exits through the outlet header. Note that the entire system is axisymmetric.

2.3 Governing Equations

The most general mathematical basis for any flow calculation is formed by the Navier-Stokes equations [13]:
Conservation of momentum

$$\frac{D\vec{v}}{Dt} = \frac{\partial \vec{v}}{\partial t} + \vec{v} \cdot \nabla \vec{v} = -\frac{1}{\rho}\nabla p + \frac{1}{\rho}\vec{f} + \frac{1}{\rho}\nabla \cdot \bar{\bar{\tau}} \tag{2.2}$$

Conservation of mass

$$\frac{\partial \rho}{\partial t} + \nabla \cdot (\rho \vec{v}) = 0 \tag{2.3}$$

in which $\vec{v}$ is the velocity vector, $\vec{f}$ is an external force (gravity for example), $\bar{\bar{\tau}}$ is the stress tensor, p is the pressure and ρ the density of the fuel salt.
This research focuses on finding a description of the core flow field assuming a constant density[*] with pumps driving the flow. Most reactor designs undergoing research today still rely on pumps and the effects of a non-uniform density on the flow field will be small because of the small pressure drops.
Using the assumption of a constant density, Eq. 2.3 can be written as:

$$\nabla \cdot \vec{v} = 0 \tag{2.4}$$

In the lower dividing plenum the flow is directed radially inward by skirts, Fig. 1.2, preventing azimuthal flow. For the upper combining plenum the same holds. It is therefore assumed that the field is axisymmetric, that the velocity only has components in the radial (r) and the axial (z) directions and that the effects of flow in the azimuthal (ϕ) direction will be negligible.
The continuity equation may be used to rewrite the advective term $\vec{v} \cdot \nabla \vec{v}$ in Eq. 2.2 in a conservative way:

$$\vec{v} \cdot \nabla \vec{v} + \vec{v} \nabla \cdot \vec{v} = \nabla \cdot \vec{v}\vec{v} \tag{2.5}$$

Since there are no external forces present one may rewrite Eq. 2.2, using the above assumptions:

$$\frac{\partial \vec{v}}{\partial t} + \nabla \cdot \vec{v}\vec{v} = -\frac{1}{\rho}\nabla p + \frac{1}{\rho}\nabla \cdot \bar{\bar{\tau}} \tag{2.6}$$

The governing equations for the remainder of this thesis, written in terms of their spatial components, [12] [3], therefore become:
Radial momentum:

$$\rho\frac{\partial u}{\partial t} + \rho\frac{1}{r}\frac{\partial r u u}{\partial r} + \rho\frac{\partial u w}{\partial z} = -\frac{\partial p}{\partial r} + [\nabla \cdot \bar{\bar{\tau}}]_r \tag{2.7}$$

---

[*] One might argue that having detailed knowledge about local densities in the reactor core is highly important since cross sections, heat transfer properties and moderation all depend on density. These effects may be calculated with existing coupled thermo-hydraulics and neutronics codes and the effect of convective precursor transport may be superimposed.

Axial momentum:

$$\rho\frac{\partial w}{\partial t}+\rho\frac{1}{r}\frac{\partial rwu}{\partial r}+\rho\frac{\partial ww}{\partial z}=-\frac{\partial p}{\partial z}+[\nabla\cdot\bar{\bar{\tau}}]_z \tag{2.8}$$

Conservation of mass:

$$\frac{1}{r}\frac{\partial ru}{\partial r}+\frac{\partial w}{\partial z}=0 \tag{2.9}$$

in which u represents the velocity in the radial direction and w the velocity in the vertical direction.
The stress terms are intentionally not written out explicitly because they will be treated in more detail later on.

2.4 Application of the governing equations

Let us revisit the equations derived in section 2.3 and apply them to the zones identified in Fig. 2.2.
Due to the complicated geometry of manifold systems such as the one investigated in this thesis it is common practice in the field to resort to empirical relations describing losses due to stresses. These relations will be derived for each zone in Fig. 2.2 individually in the following.

2.4.1 The lower dividing plenum (zone 1)

Since the aim of this report is to model the flow through the reactor core, details of the flow field in the plenums, where no fission takes place, are of secondary importance. As a further simplification it is therefore assumed that the radial velocity component can be averaged over the height of the plenum in the following way:

$$\langle u\rangle=\langle u(r)\rangle_z=\frac{1}{\triangle z}\int_{\triangle z}u(r,z)dz \tag{2.10}$$

The radial velocity component in the plenums is for the remainder of this report therefore only a function of the radial position r.

Treatment of the stresses

At the entrance of a fuel channel the concept of a single averaged radial velocity component becomes a little shaky due to turning of the flow at the branch point. The fluid will lose some of its radial momentum upon entering the fuel channel; we expect $u(branchpoint)\leq\langle u\rangle$. A static pressure regain coefficient γ_l is therefore introduced to account for an uncertainty of radial momentum transported across the interface between lower plenum and reactor core. The cross term in the axial momentum equation is modified in the following way:

$$\rho\gamma_l\frac{\partial\langle u\rangle w}{\partial z} \tag{2.11}$$

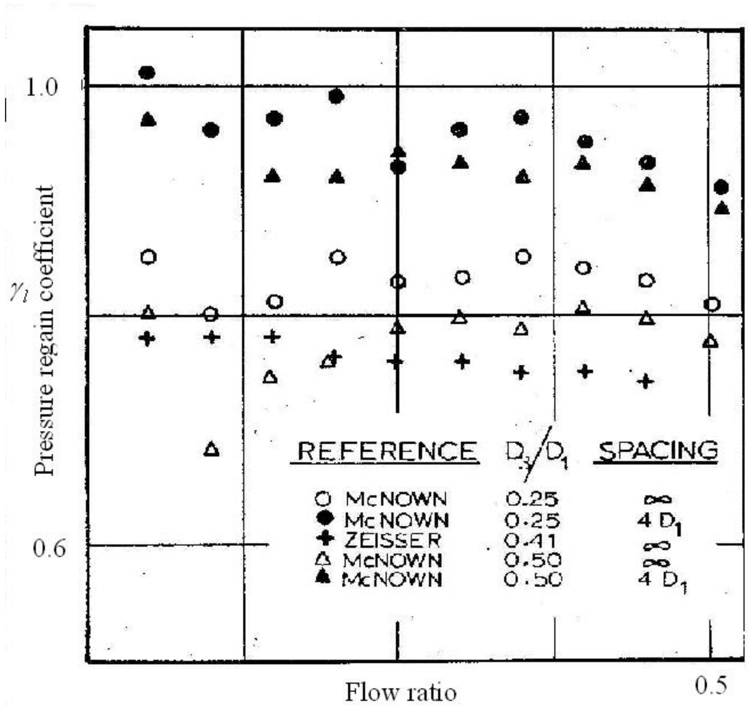

Figure 2.4: Some experimental values of the pressure regain coefficient as a function of flow ratio; the ratio between the flow into the channel and the flow through the manifold. D_3/D_1 represents the ratio between the diameter of the channel and the diameter of the manifold. The spacing indicates how far the respective channels are placed apart.

Some experimental values for γ_l are shown in Fig. 2.4. These results were obtained using a tube manifold instead of a dividing plenum [9]. The pressure regain coefficient however, appears to be insensitive to the diameter ratio of channel and manifold (or channel and plenum). It is therefore safe to use the experimental data of Fig. 2.4 for the current situation. The results indicate that γ_l increases by about 20% as the spacing between adjacent channels is decreased. The flow ratio between channels and dividing manifold also hardly influence the pressure regain coefficient. A value of $\gamma_l = 0.95$ was chosen, corresponding to the fluid leaving the plenum loosing little radial momentum.

There will of course be pressure losses due to wall shear stress. The differential pressure drop due to wall shear stress can be written as [15]:

$$\frac{\partial p}{\partial r} = -4f(Re)\rho\langle u\rangle\frac{|\,\langle u\rangle\,|}{2D_h} \tag{2.12}$$

In which $f(Re)$ is the Fanning friction factor which is a function of the Reynolds number and D_h the hydraulic diameter.

$$Re = \frac{\rho\langle u\rangle D}{\mu} \tag{2.13}$$

$$D_h = \frac{4A}{S} = \frac{8\pi r \triangle z}{4\pi r} = 2\triangle z \tag{2.14}$$

Using the empirical relations for the friction factor $f(Re)$ [15]:
Laminar regime

$$4f = \frac{64}{Re} \qquad \text{for } Re < 2000 \tag{2.15}$$

Turbulent regime

$$4f = 0.316Re^{-0.25} \qquad \text{for } 2000 < Re < 10^5 \tag{2.16}$$

The final radial momentum equation for the lower dividing plenum becomes:

$$\frac{\partial\langle u\rangle}{\partial t} + \frac{1}{r}\frac{\partial r\langle u\rangle\langle u\rangle}{\partial r} + \gamma_l\frac{\partial\langle u\rangle w}{\partial z} = -\frac{1}{\rho}\frac{\partial p}{\partial r} - 4f\langle u\rangle\frac{\mid\langle u\rangle\mid}{2\triangle z} \tag{2.17}$$

2.4.2 The reactor core (zone 2)

The fuel channels in the reactor core are very long in comparison with the width of the channels. It is therefore safe to assume that the flow is essentially vertical in zone 2 and any cross flow can be neglected. Furthermore, since the flow is incompressible, the velocity of the salt at the entrance of a fuel channel will equal the velocity at the outflow and therefore the convective term $\rho\frac{\partial ww}{\partial z}$ can be discarded. Using the above assumptions one can write Eq. 2.8 as:
Axial momentum in zone 2:

$$\rho\frac{\partial w}{\partial t} = -\frac{\partial p}{\partial z} + [\nabla \cdot \bar{\bar{\tau}}]_z \tag{2.18}$$

Stress term treatment

Inside the channels the stresses are characterized by wall the shear stress: Eq. 2.12. The area perpendicular to the flow is just the porosity times the differential area of the top of the lower plenum, or recalling Fig. 2.3, the yellow area.
Keeping Fig. 2.3 in mind, one can define a parameter describing the ratio between the wetted perimeter of all the channels divided by the total area of the top of the lower plenum (the inside edges of the yellow areas divided by the yellow and black area):

$$\beta = \frac{\text{total wetted perimeter of channels}}{\text{total are of top of lower plenum}} \tag{2.19}$$

The hydraulic diameter then becomes[†]:

$$D_h = \frac{4\alpha}{\beta} \tag{2.20}$$

The final axial momentum equation for the reactor core now reads:

$$\rho\frac{\partial w}{\partial t} = -\frac{\partial p}{\partial z} - 4f\rho w\frac{\beta\mid w\mid}{8\alpha} \tag{2.21}$$

[†] For the case of the MSRE setup the hydraulic diameter is $D_h = 1.67cm$

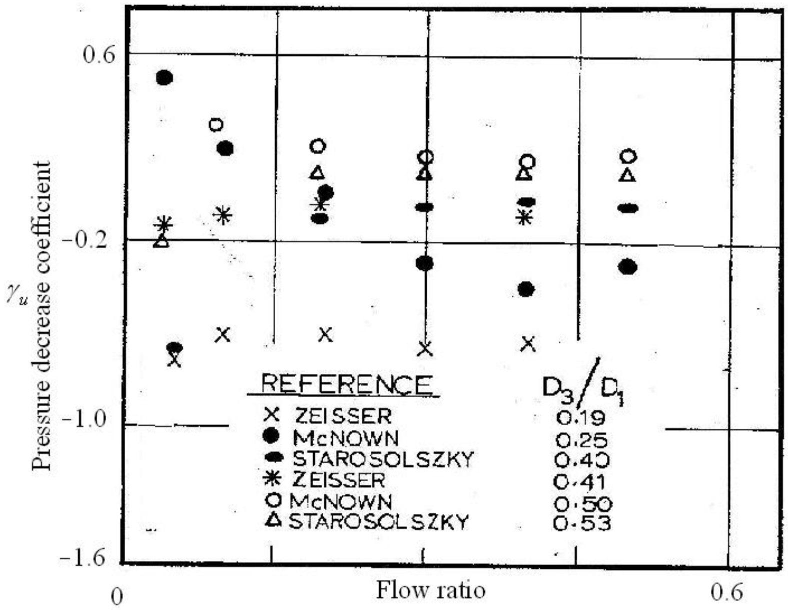

Figure 2.5: Some experimental values of the pressure decrease coefficient γ_u as a function of the flow ratio between channel and combining flow manifold.

2.4.3 The upper combining plenum (zone 3)

Stress term treatment

For the upper combining plenum, zone 3, it is also assumed that a single radial velocity $\langle u\rangle$ describes the radial flow.

A pressure decrease coefficient γ_u is introduced to account for the uncertainty of radial momentum transported across the boundary of zone 2 and 3.

$$\gamma_u \frac{\partial \langle u\rangle w}{\partial z} \tag{2.22}$$

One might expect, from symmetry considerations, the pressure regain coefficient to be equal to the pressure decrease coefficient. In the combining plenum however, the interaction of the fluid streams at the branch point is different from the dividing case.

In the dividing plenum, fluid is accelerated into the channel while leaving the remainder of the flow field unaffected, except for the expansion downstream [2]. In the combining case however, the outflow from the channels pierces the whole flow field and causes increased turbulence downstream. This makes for an entirely different behavior of the pressure decrease coefficient and even allows for γ_u to become negative. A negative value of γ_u can be interpreted as the fuel salt having a radial velocity in the upstream direction upon entering the upper combining plenum.

Fig. 2.5 shows some experimental values for the pressure decrease coefficient. Again, the pressure decrease coefficient appears to be insensitive to the flow ratio. The diameter ratio for the MSRE is around 0.1 making it hard to give an accurate estimate for γ_u. A value of $\gamma_u = -0.9$ was chosen, a little below the value of *Zeisser* [9] at a ratio of 0.19.

Wall shear stress is treated as in the lower dividing plenum leading to the momentum equation for the upper combining plenum:

$$\frac{\partial\langle u\rangle}{\partial t} + \frac{1}{r}\frac{\partial r\langle u\rangle\langle u\rangle}{\partial r} + \gamma_u\frac{\partial\langle u\rangle w}{\partial z} = -\frac{1}{\rho}\frac{\partial p}{\partial r} - 4f\langle u\rangle\frac{|\,\langle u\rangle\,|}{2\triangle z} \qquad (2.23)$$

Chapter 3

Numerical Model

3.1 Introduction

In this chapter the equations derived in chapter 2 will be discretized and applied to a specified grid. The method of discretization will be discussed and the procedure used for solving the discretized system will be outlined. Also, boundary conditions are discussed.

3.2 Method of discretization

All methods of discretization have their merits but the finite volume method was chosen because it has some specific advantages over other schemes. In the finite volume scheme the spatial domain is divided into volume cells [5] [8] in which the equations are subsequently integrated. Of all discretization methods the finite volume scheme is the most physically intuitive and it keeps the programming efforts tolerable. Also, when integrating the equations over a volume, the Jacobian takes care of some of the difficulties of the apparent singularity near $r = 0$ that arises because of the use of a cylindrical coordinate system.
The grid is fully specified by:

$$\begin{array}{ll} r(i) & i = 1, 2, ..., ni \\ z(j) & j = 1, 2, 3 \end{array} \tag{3.1}$$

The scalars, like pressure, are stored at these locations. Velocity is staggered half a cell with respect to the scalars and therefore lies on the scalar cell face. Fig. 3.1 and Fig. 3.2 show how the grid is generated in some detail. In finite volume integration, flux uniformity is assumed over the cell face so the velocities for example, are a constant at the scalar cell face. It is worth recalling that $\langle u \rangle$ represents the average radial velocity in the plenum. One can therefore divide

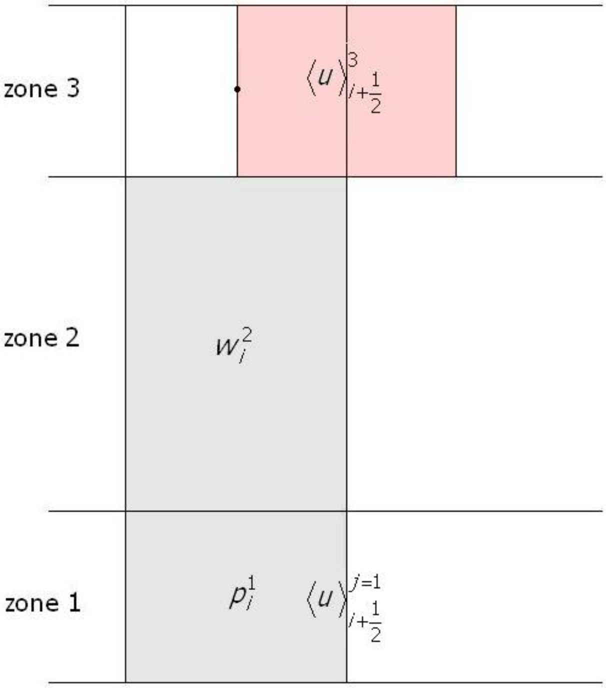

Figure 3.1: Schematic of the location of some staggered grid cells. The location of the velocity is at the edge of the scalar or continuity cell, colored grey. The momentum cell is colored light red.

the entire reactor vessel into three zones over the vertical direction ($j = 1, 2, 3$). Staggered grid arrangements, Fig. 3.1, naturally avoid odd-even pressure decoupling, [11] [8]. Also, mass conservation can be calculated more readily because no interpolation of the velocities has to be done. Whenever interpolation of velocities is necessary, the first order upwind scheme is adopted [5].

3.3 Radial momentum

The grid cell volume* shown in Fig. 3.2 is used to integrate the radial momentum equation. This equation represents the radial momentum equation for the lower dividing plenum. The treatment of the equation for the upper combining plenum is completely analogous, the only differences that need to be kept in mind are that the coefficient γ_l becomes γ_u, the porosity parameter α needs to be used for the south face of the cell area instead of the north face and the axial index j is $j = 3$ in stead of $j = 1$. Recall:

$$\frac{\partial\langle u\rangle}{\partial t} + \frac{1}{r}\frac{\partial r\langle u\rangle\langle u\rangle}{\partial r} + \gamma_l\frac{\partial\langle u\rangle w}{\partial z} = -\frac{1}{\rho}\frac{\partial p}{\partial r} - 4f\langle u\rangle\frac{\mid\langle u\rangle\mid}{2\triangle z} \tag{3.2}$$

---

[*] Both cell volume and cell face area change in the domain because of the use of cylindrical coordinates

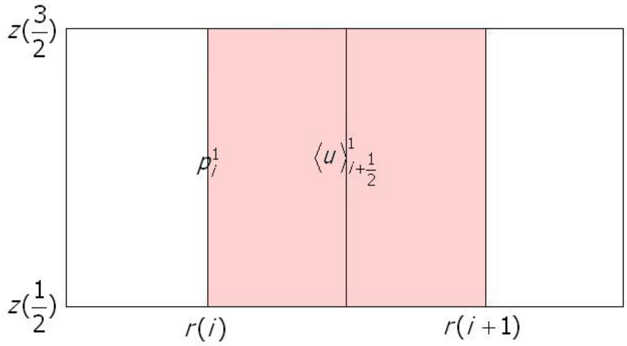

Figure 3.2: Schematic of the location of a possible radial momentum grid cell in the lower dividing plenum. The velocity is located at the momentum cell center while the pressure is located at the continuity, or scalar cell center. The integration is done over the light red area.

In the following all the terms of Eq. 3.2 are treated separately and integration is done over the radial momentum grid cell volume, which is defined as:

$$\Omega^1_{i+\frac{1}{2}} = \pi(r^2_{i+1} - r^2_i)(z_{\frac{3}{2}} - z_{\frac{1}{2}}) \tag{3.3}$$

The respective momentum cell areas are defined as:

$$a^1_{i+1} = 2\pi r_{i+1}(z_{\frac{3}{2}} - z_{\frac{1}{2}}) \tag{3.4}$$

$$a^1_i = 2\pi r_i(z_{\frac{3}{2}} - z_{\frac{1}{2}}) \tag{3.5}$$

$$a^{\frac{3}{2}}_{i+\frac{1}{2}} = \alpha\pi(r^2_{i+1} - r^2_i) \tag{3.6}$$

$$a^{\frac{1}{2}}_{i+\frac{1}{2}} = \pi(r^2_{i+1} - r^2_i) \tag{3.7}$$

3.3.1 Transient term

Integrating $\rho\frac{\partial\langle u\rangle}{\partial t}$ over the momentum cell volume results in:

$$2\pi\int_i^{i+1}\int_{\frac{1}{2}}^{\frac{3}{2}}\rho\frac{\partial\langle u\rangle}{\partial t}r\,dz\,dr = \Omega^1_{i+\frac{1}{2}}\rho\frac{\partial\langle u\rangle^1_{i+\frac{1}{2}}}{\partial t} \tag{3.8}$$

3.3.2 Advective term

Defining the mass flow as[†]:

$$\psi^j_i = \rho\vec{v}^j_i \tag{3.9}$$

[†] Note that $\vec{v}^j_i$ does not represent the true velocity vector, the notation is merely used to point out that $\vec{v}^j_i$ can represent either the radial velocity component u at some location i,j or the axial velocity component w at some location i,j

The advective terms $\frac{1}{r}\frac{\partial r\langle u\rangle\langle u\rangle}{\partial r} + \gamma_l\frac{\partial\langle u\rangle w}{\partial z}$ are integrated over the control volume, resulting in:

$$\begin{aligned}
&2\pi \textstyle\int_i^{i+1} \int_{\frac{1}{2}}^{\frac{3}{2}} (\frac{1}{r}\frac{\partial r\langle u\rangle\langle u\rangle}{\partial r} + \gamma_l\frac{\partial\langle u\rangle w}{\partial z}) r dz dr = \\
&a_{i+1}^1 \psi_{i+1}^1 \langle u\rangle_{i+1}^1 - a_i^1 \psi_i^1 \langle u\rangle_i^1 + \\
&a_{i+\frac{1}{2}}^{\frac{3}{2}} \psi_{i+\frac{1}{2}}^{\frac{3}{2}} \langle u\rangle_{i+\frac{1}{2}}^1 - a_{i+\frac{1}{2}}^{\frac{1}{2}} \psi_{i+\frac{1}{2}}^{\frac{1}{2}} \langle u\rangle_{i+\frac{1}{2}}^1
\end{aligned} \tag{3.10}$$

The south face contributions are retained despite them being zero everywhere in the lower plenum because these contributions will not be zero in the upper plenum. Since the velocities at the $(i+1,1)$, $(i,1)$ locations are unknown they are placed at the upwind positions :

$$\begin{array}{cc}
-a_{i+1}^1 \langle u\rangle_{i+\frac{3}{2}}^1 \parallel -\psi_{i+1}^1, 0 \parallel & -a_i^1 \langle u\rangle_{i-\frac{1}{2}}^1 \parallel \psi_i^1, 0 \parallel \\
+a_{i+1}^1 \langle u\rangle_{i+\frac{1}{2}}^1 \parallel \psi_{i+1}^1, 0 \parallel & +a_i^1 \langle u\rangle_{i+\frac{1}{2}}^1 \parallel -\psi_i^1, 0 \parallel \\
\multicolumn{2}{c}{a_{i+\frac{1}{2}}^{\frac{3}{2}} \langle u\rangle_{i+\frac{1}{2}}^1 \gamma_l \frac{\psi_{i+1}^{\frac{3}{2}} + \psi_i^{\frac{3}{2}}}{2} - a_{i+\frac{1}{2}}^{\frac{1}{2}} \langle u\rangle_{i+\frac{1}{2}}^1 \frac{\psi_{i+1}^{\frac{1}{2}} + \psi_i^{\frac{1}{2}}}{2}}
\end{array} \tag{3.11}$$

in which

$$\parallel a, b \parallel = \begin{cases} a & \text{if } a > b \\ b & \text{if } a \leq b \end{cases} \tag{3.12}$$

3.3.3 Pressure gradient

Integration of the pressure gradient can be approximated as:

$$2\pi \int_i^{i+1} \int_{\frac{1}{2}}^{\frac{3}{2}} \frac{\partial p}{\partial r} r dz dr = \frac{a_{i+1}^1 + a_i^1}{2}(p_{i+1}^1 - p_i^1) \tag{3.13}$$

This approximation requires some further explanation. Because of the Jacobian for cylindrical coordinates, the pressure gradient $\frac{\partial p}{\partial r}$ picks up an extra r under the integral. One has to be careful when placing the pressure point midway between the cell boundary surfaces when p would be of higher then first order in r. Suppose the pressure would be quadratic in r and the pressure point is located at r_i in a volume spanned by $r_i - \frac{\triangle r}{2} \leq r \leq r_i + \frac{\triangle r}{2}$, r_i should be located at the center of mass:

$$r_{CM} = \int_{r_i - \frac{\triangle r}{2}}^{r_i + \frac{\triangle r}{2}} r^2 dr = r_i + \frac{\triangle r}{12} \tag{3.14}$$

Putting the grid point at the midpoint between the boundaries (the easiest choice) amounts to a relative error [12] of:

$$\epsilon = \frac{\frac{\triangle r^3}{12}}{(r_i + \frac{\triangle r^2}{12 r_i}) r_i \triangle r} = \frac{1}{12i(i-1)+4} \tag{3.15}$$

What becomes clear from Eq. 3.15 is that the error dies out really fast with increasing i, but causes unacceptable errors close to $r = 0$.

When using the finite volume scheme the pressure will however not be more then linear in r and so the gradient of the pressure will be a constant. Therefore one doesn't have to account for the problems sketched above.

3.3.4 Stress term

The stress term $-4f\langle u\rangle\frac{|\langle u\rangle|}{2\triangle z}$ is integrated over the cell volume, yielding:

$$2\pi\int_{i}^{i+1}\int_{\frac{1}{2}}^{\frac{3}{2}}-4f\langle u\rangle\frac{\mid\langle u\rangle\mid}{2\triangle z}rdzdr=-4f\Omega^{1}_{i+\frac{1}{2}}\langle u\rangle^{1}_{i+\frac{1}{2}}\frac{\mid\langle u\rangle^{1}_{i+\frac{1}{2}}\mid}{2(z_{\frac{3}{2}}-z_{\frac{1}{2}})} \tag{3.16}$$

3.3.5 Summary

Gathering all terms gives the discretized radial momentum equation:

$$\begin{gathered}\Omega^{1}_{i+\frac{1}{2}}\rho\frac{\partial\langle u\rangle^{1}_{i+\frac{1}{2}}}{\partial t}-a^{1}_{i+1}\langle u\rangle^{1}_{i+\frac{3}{2}}\parallel-\psi^{1}_{i+1},0\parallel\quad-a^{1}_{i}\langle u\rangle^{1}_{i-\frac{1}{2}}\parallel\psi^{j}_{i},0\parallel\\ +a^{1}_{i+1}\langle u\rangle^{1}_{i+\frac{1}{2}}\parallel\psi^{1}_{i+1},0\parallel\quad+a^{1}_{i}\langle u\rangle^{1}_{i+\frac{1}{2}}\parallel-\psi^{1}_{i},0\parallel\\ a^{\frac{3}{2}}_{i+\frac{1}{2}}\langle u\rangle^{1}_{i+\frac{1}{2}}\gamma l\frac{\psi^{\frac{3}{2}}_{i+1}+\psi^{\frac{3}{2}}_{i}}{2}-a^{\frac{1}{2}}_{i+\frac{1}{2}}\langle u\rangle^{1}_{i+\frac{1}{2}}\frac{\psi^{\frac{1}{2}}_{i+1}+\psi^{\frac{1}{2}}_{i}}{2}\\ =-\frac{a^{1}_{i+1}+a^{1}_{i}}{2}(p^{1}_{i+1}-p^{1}_{i})-4f\Omega^{1}_{i+\frac{1}{2}}\langle u\rangle^{1}_{i+\frac{1}{2}}\frac{|\langle u\rangle^{1}_{i+\frac{1}{2}}|}{2(z_{\frac{3}{2}}-z_{\frac{1}{2}})}\end{gathered} \tag{3.17}$$

3.4 Axial momentum in the reactor core

The grid cell volume shown in Fig. 3.3 represents a portion of the 'porous' core center, zone 2, and is used to integrate the vertical momentum equation. Recall:

$$\rho\frac{\partial w}{\partial t}=-\frac{\partial p}{\partial z}-4f\rho w\frac{\beta\mid w\mid}{8\alpha} \tag{3.18}$$

In the following all the terms of Eq. 3.18 are treated separately and are integrated over the axial momentum cell volume which is defined as:

$$\Omega^{2}_{i}=\pi(r^{2}_{i+\frac{1}{2}}-r^{2}_{i-\frac{1}{2}})(z_{\frac{5}{2}}-z_{\frac{3}{2}})\alpha \tag{3.19}$$

The respective momentum cell faces are defined as:

$$a^{\frac{5}{2}}_{i}=\pi(r^{2}_{i+\frac{1}{2}}-r^{2}_{i-\frac{1}{2}})\alpha \tag{3.20}$$

$$a^{\frac{3}{2}}_{i}=\pi(r^{2}_{i+\frac{1}{2}}-r^{2}_{i-\frac{1}{2}})\alpha \tag{3.21}$$

3.4.1 Transient term

Integrating $\rho\frac{\partial w}{\partial t}$ over the grid cell volume yields:

$$2\pi\int_{i-\frac{1}{2}}^{i+\frac{1}{2}}\int_{\frac{3}{2}}^{\frac{5}{2}}\rho\frac{\partial w}{\partial t}rdzdr=\rho\Omega^{2}_{i}\frac{\partial w}{\partial t} \tag{3.22}$$

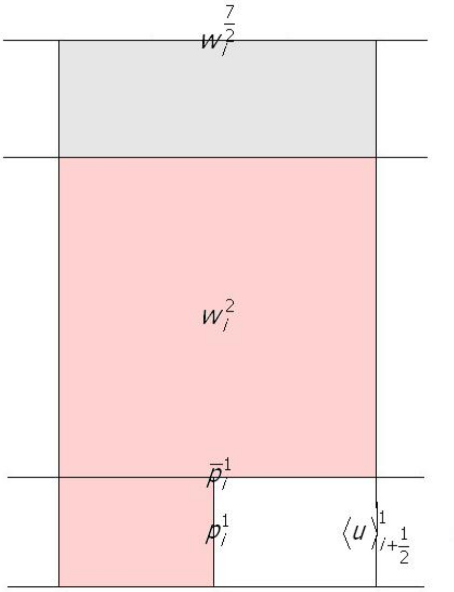

Figure 3.3: Schematic of the location of the axial momentum grid cell in the reactor core (zone 2). The velocity is located at the momentum cell center, colored light red. The pressures are located at the scalar cell centers in the upper and lower plenum, coloured grey. Integration is done over the light red area in the center of the picture. Half a radial momentum cell in the lower plenum is also drawn light red to illustrate the staggered grid arrangement. The pressure $\bar{p}_i^1$ is located at the channel entrance, while the pressure p_i^1 is located at the actual 'known' pressure point.

3.4.2 Pressure gradient

Integrating the pressure gradient over the grid cell volume yields:

$$2\pi \int_{i-\frac{1}{2}}^{i+\frac{1}{2}} \int_{\frac{3}{2}}^{\frac{5}{2}} r \frac{\partial p}{\partial z} dz dr = \frac{a_i^{\frac{5}{2}} + a_i^{\frac{3}{2}}}{2} (\bar{p}_i^{\frac{5}{2}} - \bar{p}_i^{\frac{5}{2}}) \tag{3.23}$$

There is however no pressure located at positions $(i, \frac{5}{2})$ and $(i, \frac{3}{2})$. The pressure is therefore extrapolated to the known positions $(i, 3)$ and $(i, 1)$. In doing so, some pressure losses due to turning effects will be neglected. These losses are therefore incorporated in the following way. Assume that the flow into the channel is governed by a Bernoulli equation of the following form:

$$p_i^1 - \bar{p}_i^1 = \rho(1 + T_l) \frac{w_i^2 w_i^2}{2} \tag{3.24}$$

in which $T_l > 0$ represents a coefficient describing the turning pressure loss, [2] [9]

For the boundary between core and upper combining plenum one can assume a similar relation:

$$\bar{p}_i^3 - p_i^3 = \rho(1 + T_l) \frac{w_i^2 w_i^2}{2} \tag{3.25}$$

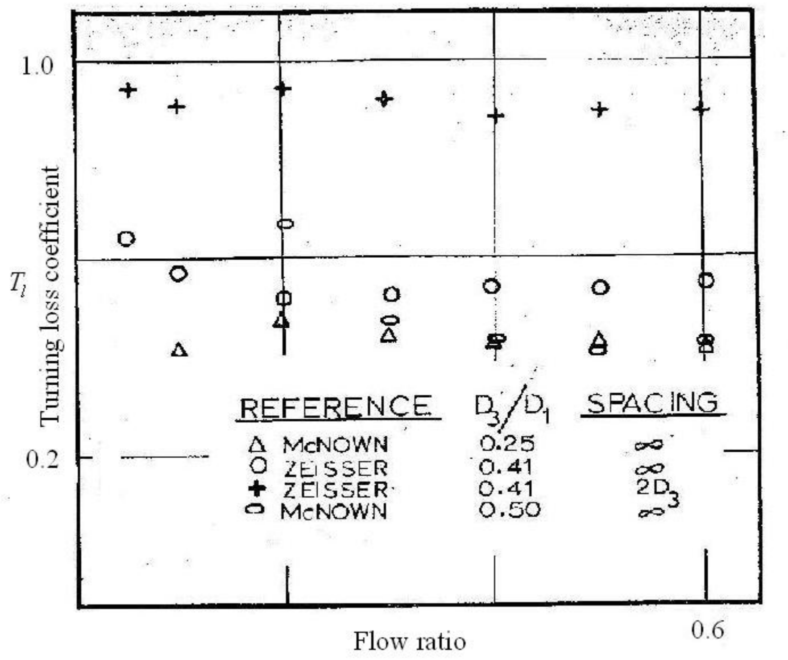

Figure 3.4: Some experimental values of the turning loss coefficient T_l as a function of the flow ratio between channel and manifold.

Fig. 3.4 shows some experimental values for the turning loss coefficient T_l obtained by using a dividing tube manifold rather than a dividing plenum. The turning loss coefficient appears to be fairly insensitive to flow ratio or tube diameter ratio but increases by some 80% as the spacing between adjacent channels is reduced. The average spacing between adjacent channels in the MSRE is about two times the channel diameter. A value of $T_l = 0.9$ for the turning loss coefficient was chosen.

Summing the contributions for inflow and outflow:

$$\overline{p}_i^3 - \overline{p}_i^1 = p_i^3 - p_i^1 + \rho(1 + T_l)w_i^2 w_i^2 \tag{3.26}$$

The pressure gradient thus becomes:

$$\frac{a_i^{\frac{5}{2}} + a_i^{\frac{3}{2}}}{2}(p_i^3 - p_i^1 + \rho(1 + T_l)w_i^2 w_i^2) \tag{3.27}$$

3.4.3 Stress term

Integrating $-4f\rho w\frac{\beta|w|}{8\lambda}$ over the cell volume yields:

$$2\pi\int_{i-\frac{1}{2}}^{i+\frac{1}{2}}\int_{\frac{3}{2}}^{\frac{5}{2}} 4f\rho\frac{\beta w^2}{8\lambda} r dz dr = 4f\Omega_i^2\rho w_i^2\frac{\beta \mid w_i^2 \mid}{8\alpha} \tag{3.28}$$

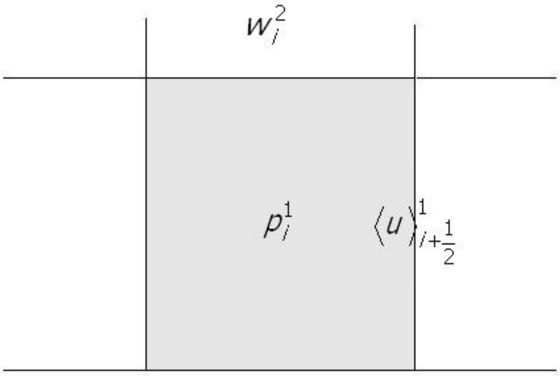

Figure 3.5: Schematic of the location of a possible continuity or scalar cell in the lower dividing plenum, coloured grey. Due to the staggered arrangement all velocities lie on the scalar cell faces.

3.4.4 Summary

Gathering terms givse the discretized axial momentum equation in the reactor core:

$$\begin{gathered}\rho\Omega_i^2\frac{\partial w_i^2}{\partial t}\\ =-\frac{a_i^{\frac{5}{2}}+a_i^{\frac{3}{2}}}{2}(p_i^3-p_i^1+\rho(1+T_l)w_i^2w_i^2)\\ -\Omega_i^2\frac{4f\rho\beta}{8\alpha}w_i^2\mid w_i^2\mid\end{gathered}\tag{3.29}$$

3.5 Continuity equation

Integration of the continuity equation, Eq. 2.9, is equivalent in every zone. No interpolation has to be done because all velocities are located at the continuity cell face as can be seen in Fig. 3.5. It is useful to write the continuity equation in terms of mass flow ψ by multiplying the velocities with the density ρ. Integrating results in:

$$2\pi\int_{i-\frac{1}{2}}^{i+\frac{1}{2}}\int_{\frac{1}{2}}^{\frac{3}{2}}\rho(\frac{1}{r}\frac{\partial ru}{\partial r}+r\frac{\partial w}{\partial z})rdzdr=a_{i+\frac{1}{2}}^1\psi_{i+\frac{1}{2}}^1-a_{i-\frac{1}{2}}^1\psi_{i-\frac{1}{2}}^1+a_i^{\frac{3}{2}}\psi_i^{\frac{3}{2}}-a_i^{\frac{1}{2}}\psi_i^{\frac{1}{2}}\tag{3.30}$$

3.6 Solution algorithm

3.6.1 Introduction

This section provides the solution algorithm used to solve the set of discretized equations derived in the previous sections. Some thoughts will be given to the time stepping procedure and an iterative solution method will be presented for the system making use of so called pressure correction equations (see [11], [8] and [12] for a detailed description of the procedure).

3.6.2 Time stepping

The time dependency of the equations derived in the previous sections still remains and needs to be handled in some way.
A time step can be defined as:

$$\triangle t = t^{n+1} - t^{n} \tag{3.31}$$

Now consider the following first order differential equation in time, equivalent to the discretized equations derived earlier:

$$\frac{dy}{dt} = f(y) \tag{3.32}$$

Since the time derivative of y is simply $lim_{\triangle t \rightarrow 0} \frac{y(t+\triangle t)-y(t)}{\triangle t}$, the left hand side of Eq. 3.32 is easily discretized. This however leaves a choice for the right hand side. The implicit scheme [5] used in this thesis places the solution variable at the new time level $t + \triangle t$, (or $n + 1$):

$$\frac{dy}{dt} = \frac{y^{n+1} - y^{n}}{\triangle t} = f(y^{n+1}) \tag{3.33}$$

The non-linearities in the discretized equations (like $w_i^2 w_i^2$) pose a problem which can be overcome by making clever use of the different steps in time. One can linearize the non-linear terms by placing one of the velocities at the old time level n. For example: $w_i^2(n+1)w_i^2(n+1) = w_i^2(n)w_i^2(n+1)$. All the non-linear terms in Eq. 3.47 and Eq. 3.17 can be linearized in this way.
For example, the axial momentum equation in the reactor core becomes:

$$\begin{gathered} \tfrac{\rho}{\triangle t}\Omega_i^2 (w(n+1)_i^2 - w(n)_i^2) \\ = -\tfrac{a_i^{\frac{5}{2}} + a_i^{\frac{3}{2}}}{2} (p(n+1)_i^3 - p(n+1)_i^1 + \rho(1+T_l) w(n+1)_i^2 w(n)_i^2) \\ -\Omega_i^2 \tfrac{4f\rho\beta}{8\alpha} \mid w(n+1)_i^2 \mid w(n+1)_i^2 \end{gathered} \tag{3.34}$$

The equations now represent a linear set. To ease notation, all variables are gathered into algebraic vectors $\vec{p}$, $\vec{v} = (u, w)$, and all coefficients are gathered in operators $\overline{\overline{D}}$ (convection and friction), $\overline{\overline{L}}$ (divergence) and $\overline{\overline{Q}}$ (gradient) acting on these vectors. In doing so, the system to be solved becomes:
Momentum

$$\frac{\rho}{\triangle t}(\vec{v}^{n+1} - \vec{v}^{n}) = \overline{\overline{D}}\vec{v}^{n+1} - \overline{\overline{Q}}\vec{p}^{n+1} \tag{3.35}$$

Mass conservation

$$\overline{\overline{L}}\vec{v}^{n+1} = 0 \tag{3.36}$$

3.6.3 Pressure correction

What becomes clear from Eq. 3.35 and Eq. 3.36 is that unless some pressure field is specified, it is impossible to solve the set of equations. The pressure field has to be estimated, and unless the correct field is applied, the resulting velocity field will not fulfill mass conservation.

The so called pressure correction scheme is adopted, [11] [12] [8]. The goal is to improve the guessed pressure such that the resulting velocity field will get progressively closer to satisfying the continuity equation.

First a guessed velocity field $\vec{v}^*$ is calculated using the old time level pressure $\vec{p}^n$.

$$\frac{\rho}{\triangle t}(\vec{v}^* - \vec{v}^n) = \overline{\overline{D}}\vec{v}^* - \overline{\overline{Q}}\vec{p}^n \tag{3.37}$$

In general, this velocity field will not satisfy mass conservation.

$$\overline{\overline{L}}\vec{v}^* = \vec{\epsilon} \neq 0 \tag{3.38}$$

Now suppose that the 'true' pressure can be written as the pressure at the old time level n plus a pressure correction $\delta\vec{p}$:

$$\vec{p}^{n+1} = \vec{p}^n + \delta\vec{p} \tag{3.39}$$

Subtracting Eq. 3.37 from Eq. 3.35 then results in a momentum equation for the pressure corrections,

$$\frac{\rho}{\triangle t}\delta\vec{v} = -\overline{\overline{Q}}\delta\vec{p} \tag{3.40}$$

in which $\overline{\overline{D}}\delta\vec{v}$ is neglected. In making this assumption it is assumed that the velocity correction is fully caused[‡] by the correction in the pressure.

Enforcing continuity ($\overline{\overline{L}}\delta\vec{v} = -\vec{\epsilon}$) results in a Poisson-like system (linear and symmetric) with boundary conditions fully determined by the discretization of the momentum equations:

$$\overline{\overline{LQ}}\delta\vec{p} = \frac{\rho}{\triangle t}\overline{\overline{L}}\vec{v}^* \tag{3.41}$$

Finally the pressure and velocity are updated using:

$$\vec{p}^{n+1} = \vec{p}^n + \delta\vec{p} \tag{3.42}$$

$$\vec{v}^{n+1} = \vec{v}^* + \frac{\triangle t}{\rho}\overline{\overline{Q}}\delta\vec{p} \tag{3.43}$$

The new velocity field will fulfill mass conservation if the pressure correction is performed accurately enough.

[‡] It can be shown that in doing so, the order of accuracy isn't affected.

3.6.4 Summary

The whole procedure can be summarized by the following steps:

1: Solve the momentum equations Eq. 3.37 to obtain the guessed velocity field $\vec{v}^*$.

2: Solve the pressure correction equation Eq. 3.41 to obtain $\vec{\delta p}$.

3: Update the pressure and velocity fields with Eq. 3.42 and Eq. 3.43.

4: Return to step 1, taking the updated pressure as the old level and repeat until the pressure and velocity fields are converged to obtain the steady state solution, or save at every time step to track the solution in real time (transient simulation) and return to step 1 until some specified time is reached.

To check for convergence, the pressure corrections for all cells are added. If this sum of pressure corrections is sufficiently close to zero, the loop is terminated. As an extra precaution the velocity of one cell is tracked during the procedure to see whether it is converging or not. Furthermore, the mass error of each cell should be zero after correction and the flow rate at the intake should equal the flow rate at the outlet and the integral of the flow over the channels in the reactor core.

3.7 Boundary Conditions

3.7.1 Introduction

Four different boundaries can be identified which are of particular interest for the numerical treatment of the equations. These boundaries are specified in Fig. 3.6 and will be treated below.

3.7.2 Boundaries with specified velocity

The inflow boundary is marked by 1 in Fig. 3.6 and is located at $(i = ni + \frac{1}{2}, j = 1)$. The flow rate at that location is given and therefore the velocity is specified at that location: $u^1_{ni+\frac{1}{2}} = u_{in}$. The system to be solved can, for example, be written as[§].

$$\overline{\overline{A}}\vec{v}^{n+1} = \vec{S}^n \tag{3.44}$$

To meet the condition that the inflow velocity remains the same throughout the whole procedure, one simply makes the coefficient in $\overline{\overline{A}}$ corresponding to the

---

[§] $\overline{\overline{A}}$ is not specified at all in this case because it is only used to demonstrate how one can meet the boundary conditions

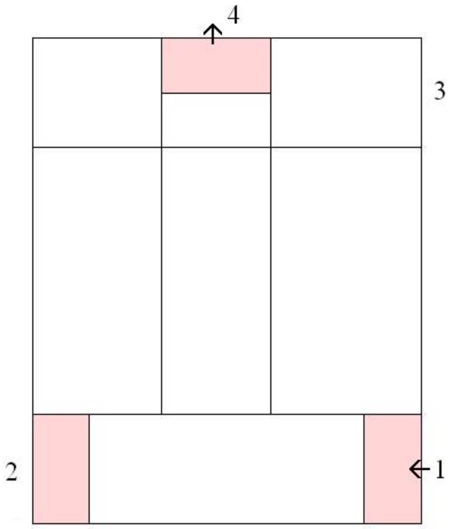

Figure 3.6: Overview of the different boundaries which are of particular interest for the discretization of the equations. The inflow boundary is marked by the number 1, the center of symmetry boundary by 2, the no in- or outflow boundary by 3 and the outflow boundary by 4. Boundaries 1,2 and 3 can all be treated alike since the velocity is specified at these locations, see section 3.7.2 for details.

inflow velocity equal to 1 and all others in that row 0.

$$\begin{pmatrix} 1 & 0 & \cdots \\ a_{21} & a_{22} & \cdots \\ \vdots & \vdots & \ddots \end{pmatrix} \begin{pmatrix} \langle u(n+1)\rangle^{1}_{ni+\frac{1}{2}} \\ \vdots \\ \vdots \end{pmatrix} = \begin{pmatrix} u_{in} \\ \vdots \\ \vdots \end{pmatrix} \tag{3.45}$$

All boundaries in which the velocity is specified, also wall boundaries since the velocity there is zero, are treated analogously.

3.7.3 Outflow boundary

To be able to solve the equations, either the pressure or the velocity in the outflow has to be specified. Specifying the velocity will lead to a similar boundary treatment as was done in section 3.7.2. Specifying the pressure is however a more natural way of handling the boundary condition and is therefore common practice [11].

The whole flow field only depends on the gradient of the pressure; adding or subtracting an arbitrarily large number to the pressure wouldn't make a difference. At some point, an absolute pressure has to be specified somewhere in the system otherwise the pressure correction system Eq. 3.41 would become singular. Defining the pressure in the outflow automatically prevents this problem from

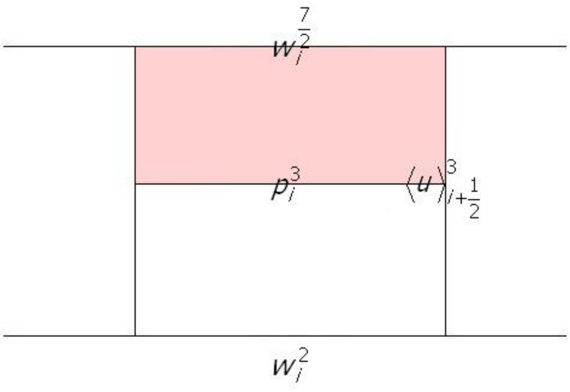

Figure 3.7: Schematic of a possible outflow grid cell in the upper combining plenum, boundary 4, in a little more detail.

occurring.
Recall the axial momentum equation:

$$\rho\frac{\partial w}{\partial t} + \rho\frac{1}{r}\frac{\partial rwu}{\partial r} + \rho\frac{\partial ww}{\partial z} = -\frac{\partial p}{\partial z} + [\nabla \cdot \overset{=}{tau}]_z; \tag{3.46}$$

Integrating over the control volume specified in Fig. 3.7 and neglecting the associated stresses yields:

$$\begin{array}{cc}
\multicolumn{2}{c}{\frac{\rho}{\triangle t}\Omega_i^3(w(n+1)_i^{\frac{7}{2}} - w(n)_i^{\frac{7}{2}})} \\
\multicolumn{2}{c}{a_i^{\frac{7}{2}} w(n+1)_i^{\frac{7}{2}} \psi(n)_i^{\frac{7}{2}}} \\
+a_i^3 w(n+1)_i^{\frac{7}{2}} \parallel -\psi(n)_i^3, 0 \parallel & -a_i^3 w(n+1)_i^3 \parallel \psi(n)_i^3, 0 \parallel \\
-\frac{a^3_{i+\frac{1}{2}}}{2} w(n+1)_{i+1}^{\frac{7}{2}} \parallel -\psi(n)_{i+\frac{1}{2}}^3, 0 \parallel & +\frac{a^3_{i+\frac{1}{2}}}{2} w(n+1)_i^{\frac{7}{2}} \parallel \psi(n)_{i+\frac{1}{2}}^3, 0 \parallel \\
-\frac{a^3_{i-\frac{1}{2}}}{2} w(n+1)_{i-1}^{\frac{7}{2}} \parallel \psi(n)_{i-\frac{1}{2}}^3, 0 \parallel & +\frac{a^{j+2}_{i-\frac{1}{2}}}{2} w(n+1)_i^{\frac{7}{2}} \parallel -\psi(n)_{i-\frac{1}{2}}^3, 0 \parallel \\
\multicolumn{2}{c}{= -\frac{a_i^{\frac{7}{2}} + a_i^3}{2}(p(n+1)_{\text{out}} - p(n+1)_i^3}
\end{array} \tag{3.47}$$

Note that the outflow equation exhibits several differences in comparison with Eq. 3.47. First of all, both convective terms are retained which wasn't the case in the description of the flow in the channels. Furthermore the cell volume is half the regular volume, the pressure at the outlet is specified and the stresses are neglected.

Chapter 4

Benchmark checks

4.1 Introduction

In this chapter some checks will be performed to verify the validity of the proposed physical and numerical models. First a version of the model in Cartesian coordinates is presented and used to simulate the flow field in a parallel flow manifold. Second, an infinite resistance check is performed to validate if a uniform distribution of salt amongst the channels in the reactor core is predicted by the code. And third, a check is performed whether the code produces equivalent results when altering mesh size.

4.2 Benchmark: Parallel flow manifold

4.2.1 Introduction

In [9], experiments were performed using a tube parallel flow manifold of which a schematic is presented in Fig. 4.1. Other than the MSRE, in which the plenums are curved cylinders, the parallel tube manifold consists of two tubes separated by twenty channels. Each channel houses a resistance orifice which can be opened or closed to decrease or increase axial flow resistance. The obtained experimental values can be used to verify the validity of the procedure presented in this thesis. In the following, slightly modified working equations will be presented and the results will be compared with the results obtained in [9].

4.2.2 Governing equations

The starting point as before are the conservative Navier Stokes equations; Eq. 2.4 and Eq. 2.6. This time, however, the equations are written out in their Cartesian components [3], rather then the cylindrical components used to describe

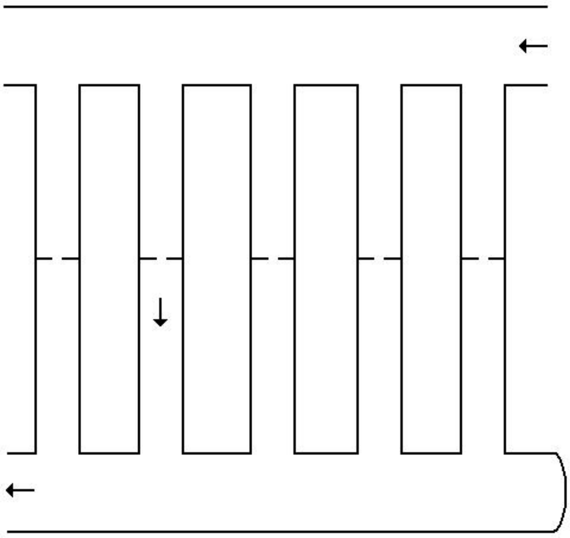

Figure 4.1: Schematic of the experimental apparatus used by Bajura to obtain measurements of a parallel flow manifold. In the benchmark performed here, the apparatus houses 20 channels of $3.18cm$ diameter and $1.56m$ height, separated by a distance of $25.91cm$. Both combining and dividing tube manifolds have a length of $5.18m$ and a diameter of $10.16cm$. All channels contain a resistance orifice the control axial flow resistance.

the MSRE. Along the same lines of chapter 2, the working equations for this benchmark can be derived:

Conservation of momentum in the manifolds

$$\frac{\partial\langle u\rangle}{\partial t}+\frac{\partial\langle u\rangle\langle u\rangle}{\partial x}+\gamma_l\frac{\partial\langle u\rangle w}{\partial z}=-\frac{\partial p}{\partial x}-4f\langle u\rangle\frac{\langle\mid u\rangle\mid}{2\triangle z} \tag{4.1}$$

Conservation of momentum in the channels

$$\rho\frac{\partial w}{\partial t}+\rho\frac{\partial ww}{\partial z}=-\frac{\partial p}{\partial z}-4f\rho w\frac{\beta\mid w\mid}{8\lambda} \tag{4.2}$$

Conservation of mass

$$\frac{\partial u}{\partial x}+\frac{\partial w}{\partial z}=0 \tag{4.3}$$

Flow into and from the channels

$$\begin{aligned} p-\overline{p}&=\rho(1+T_l)\tfrac{w^2}{2}\\ \overline{p}-p&=\rho(1+T_l)\tfrac{w^2}{2}\end{aligned} \tag{4.4}$$

Note the similarity between the Cartesian equations presented here and the cylindrical equations derived in chapter two. The main difference between the two sets of equations lies in the non-constant geometrical coefficients and the apparent singularity at $r=0$. The parameters λ and β are defined as before; Eq. 2.19 and

Eq. 2.1. The discretization of the equations is completely analogous and requires no further elaboration here.
Some relevant parameters for the experimental setup are listed below.

Manifold lenghth	$L = 5.18m$
Porosity	$\alpha = 0.02757$
Perimeter ratio	$\beta = 2.87$
No. of channels	20
Turning loss	$T_l = 12$

4.2.3 Results and discussion

Below, the results of an experiment performed in [9] and the results obtained by the Cartesian code are compared. A grid size of 50 points in the radial direction was used and 20 measurement points were obtained in [9].
From Fig. 4.2 it becomes clear that the code provides results (black line) that are in rather good agreement with the experimental data (red dots) close to the beginning of the manifold system, but the code exaggerates the pressure difference between dividing and combining manifold near the end of the system. Since the square root of the pressure difference between combining and dividing manifold is a measure of the discharge of liquid, the code will also overestimate the discharge at branch points closer to the end of the manifold, although to a lesser extent than Fig. 4.2 suggests.
The difference might come from the fact that the code seems to underestimate the pressure regain due to the discharge in the lateral channels of the dividing manifold, a result which was obtained from another calculation. One possible explanation for this behavior might be that it was very hard in this situation to make an estimate of the pressure regain and pressure loss coefficients from the available data.

4.3 Infinite resistance

4.3.1 Introduction

In this section a computation is performed to verify whether the code will provide the correct result corresponding to the outcome of a known situation. If the resistance in the reactor core is infinite, all other loss mechanisms become negligible and continuity will guarantee that the velocity of the salt will be equal for every channel. Also, because the discharge will be constant, the gradient in the velocity of the lower plenum will be constant. The parameters used for the calculations are listed in table 5.1.

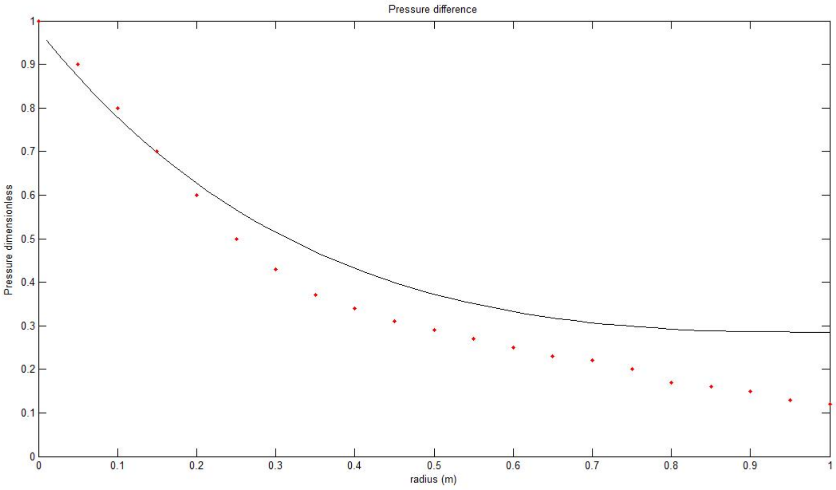

Figure 4.2: Both the results of [9], depicted as red dots, and the results of the code, depicted as a black line, are plotted. The dimensionless pressure is defined as the pressure difference between combining and dividing flow manifold divided by the total pressure drop over the system. The dimensionless distance is defined as the distance from the exit of the combining manifold divided by the total length of the manifold.

4.3.2 Results and discussion

For each cell in the reactor core, zone 2, the resistance was multiplied by a factor of 10^8. A calculation of the steady state velocity profiles resulted in Fig. 4.3. Some relevant parameters for the calculations done in the following benchmarks are listed in 5.1. The results in Fig. 4.3 clearly show that the code provides the expected outcome. From further calculations it followed that the discharge becomes gradually more uniformly distributed over the reactor core when increasing the resistance, but increasing the resistance multiplication above a factor of 10^8 leads to an unacceptable decrease in convergence time.

4.4 Grid size comparison

4.4.1 Introduction

A good way of validating if a code works correctly is to check whether the code produces similar results using a different number of grid points for the same geometry. Of course there will be some differences because a coarser grid will generally yield a less accurate result, but the overall shape of the velocity and pressure field should be similar.

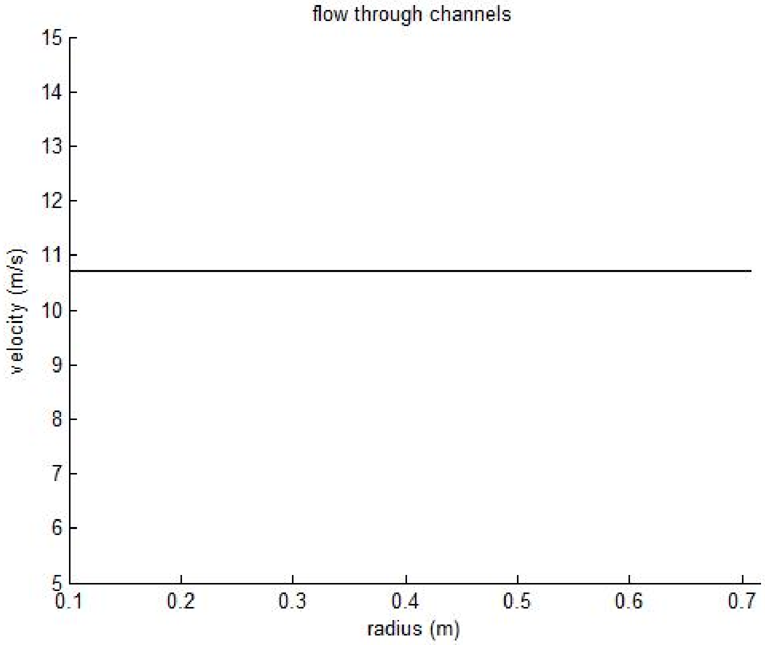

Figure 4.3: The axial velocity in the reactor core as a function of the radial distance from the center of the core. The resistance is multiplied by a factor of 10^8.

4.4.2 Results and discussion

In Fig. 4.4 the results of calculations with a mesh size of respectively 50, 100 and 150 grid points in the radial direction at a nominal flow rate of $g_{nom} = 0.80247 m^3/s$ are shown. Fig. 4.4 shows that the code produces results that are almost mesh size independent. The variations between the different graphs stem mostly from the definition of the outflow boundary. The upper boundary is discretized resulting in two possibilities; either the boundary is wall or the boundary is outflow. The cells closest to the transition between wall or outflow determine how much of the outflow is seen by the code. This problem is illustrated in Fig. 4.5. For further calculations a grid size of 180 is chosen because this covers the outflow completely and gives an acceptable convergence time.

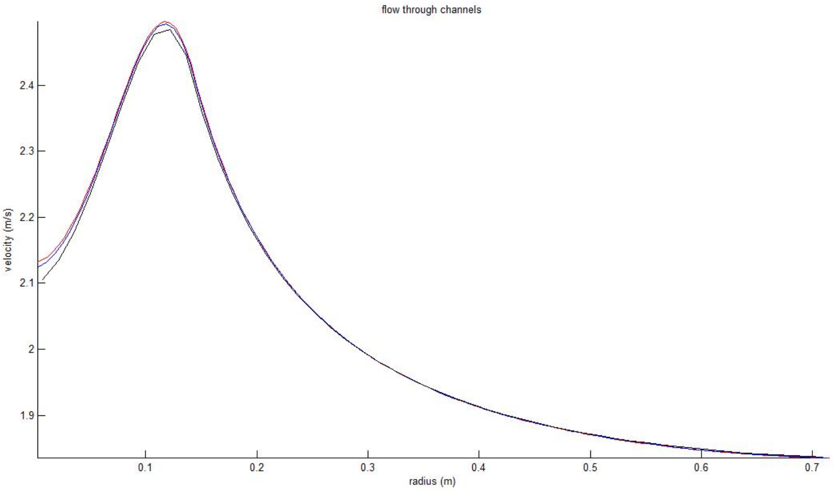

Figure 4.4: The axial velocity in the reactor core as a function of the radial distance form the center of the core plotted for three different grid sizes. The red line represents a grid size of 180, the blue line 100 and the black line 50. Calculations are performed at the nominal flow rate for the MSRE.

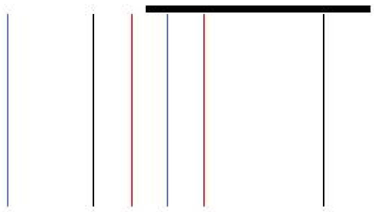

Figure 4.5: Schematic of the transition between wall and outflow in the upper combining plenum. The red lines represent the finest mesh size, blue the coarder, and black the coarsest. Choosing a grid size of 180 cells in the radial direction will ensure that the outflow is fully filled.

Chapter 5

Results and discussion

5.1 Introduction

In this chapter the computational results obtained by the code will be presented. First a computation is made for the nominal flow rate of the MSRE setup and detailed results of the pressure profiles and flow rates in the plenums are discussed. Second, calculations at different flow rates are performed to see how the discharge profile changes with various intake velocities and third, a start up transient is simulated. In the final sections of this chapter some thought will be given to the sensitivity of the code to the various model parameters and problems concerning the validity of the code will be discussed. The relevant parameters used for the calculations of this chapter are listed below in below in table5.1.

Maximum radius from core center	$L = 0.717m$
Plenum height	$H_p = 0.3302m$
Channel height	$H_c = 1.677$
Edge of outlet header, from core center	$D = 0.143m$
Turning loss	$T_l = 0.9$
Porosity	$\lambda = 0.25814$
Perimeter ratio	$\beta = 61.82m^{-1}$
Pressure regain	$\gamma_l = 0.95$
Pressure loss	$\gamma_u = -0.9$
Inflow	$g_{nom} = 0.80247m^3/s$
Density	$\rho = 2283.8kg/m^3$
Viscosity	$\mu = 7.738mPas$
Outlet pressure	$p_{out} = 0Pa$
Number of cells in radial direction	$ni = 180$

(5.1)

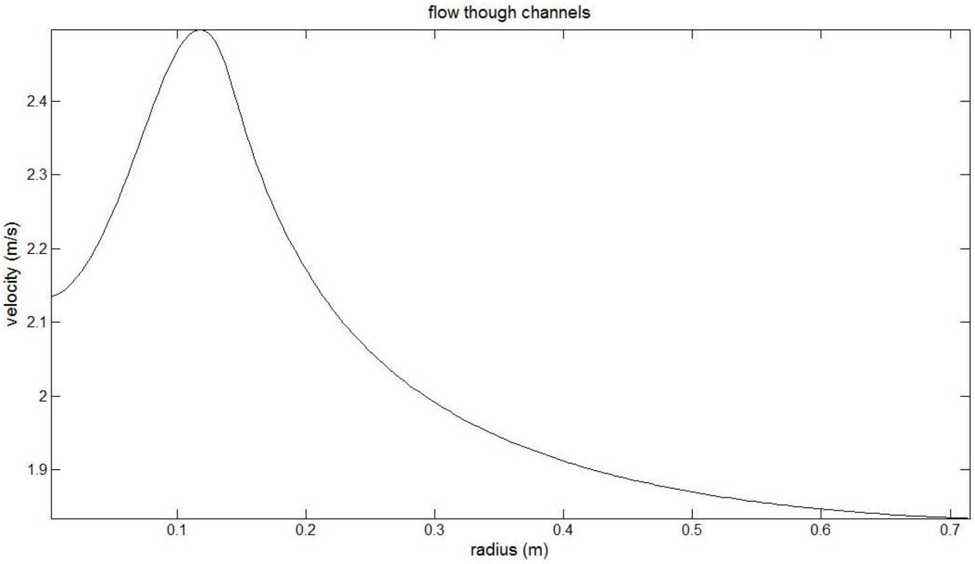

Figure 5.1: Axial velocity field in the center, zone 2, of the MSR core at nominal flow rate. Calculation are performed with the parameters specified in 5.1.

5.2 Computations at nominal flow rate

The flow rate at which the MSRE setup operated most of the time is $g_{nom} = 0.80247m^3/s$. The results obtained by the code are made visible in Fig. 5.1 (axial velocity distribution in the reactor core zone 2), Fig. 5.2 (pressure profiles in lower and upper plenum), Fig. 5.3 (pressure difference between the plenums and pressure difference between upper plenum and outflow) and Fig. 5.4 (radial velocity profiles in the plenums). Although the axial velocity distribution is the main interest of this research some interesting insights may be inferred from the other figures as well. From Fig. 5.1 it can be seen that the deviation from a constant velocity profile can become substantial at nominal flow. The highest velocity is some 30% greater than the lowest velocity calculated at steady state. The axial velocity in the channels gradually increases when going from the outside, $r = r_{max}$, of zone 2 to the inside at $r = 0$. A maximum is reached just before the point at which the outlet header at $r = 0.143m$ starts, after which the velocity decreases due to the influence of the header. The pressure difference between the plenums, Fig. 5.3 (1^{st} figure), can be interpreted as a measure for the axial velocity in zone 2 because it acts as a driving term in the axial momentum equation and the shape is therefore comparable. It is interesting to note here that the axial velocity distribution, Fig. 5.1, follows the same line as the discharge in the parallel flow manifold Fig. 4.2 up until the point where the outflow comes into play. Although an entirely different apparatus, the same physical phenomena are responsible.

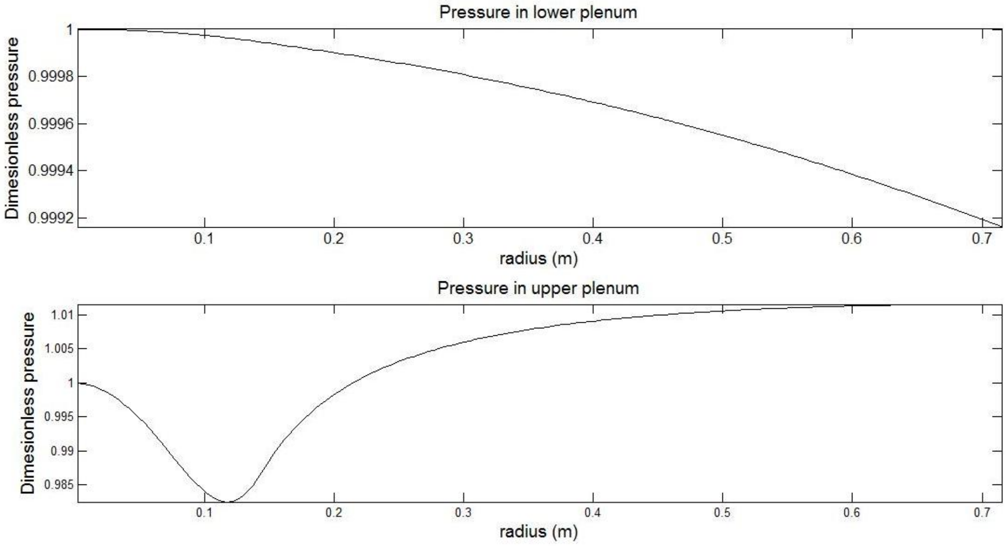

Figure 5.2: Pressure field in the plenums of the MSRE setup at nominal flow rate. The pressure is normalized with respect to the pressure point closest to the center of the core, $r = 0$, in the respective plenum.

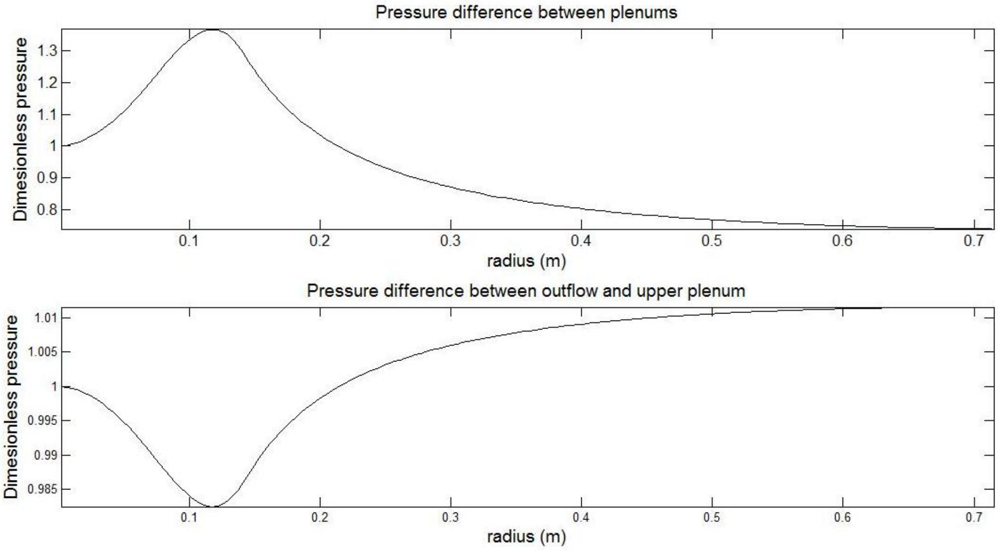

Figure 5.3: Pressure difference between the plenums and pressure difference between upper combining plenum and outflow at nominal flow rate. Pressures are normalized with respect to the pressure difference between points closest to the center, $r = 0$, of the reactor core.

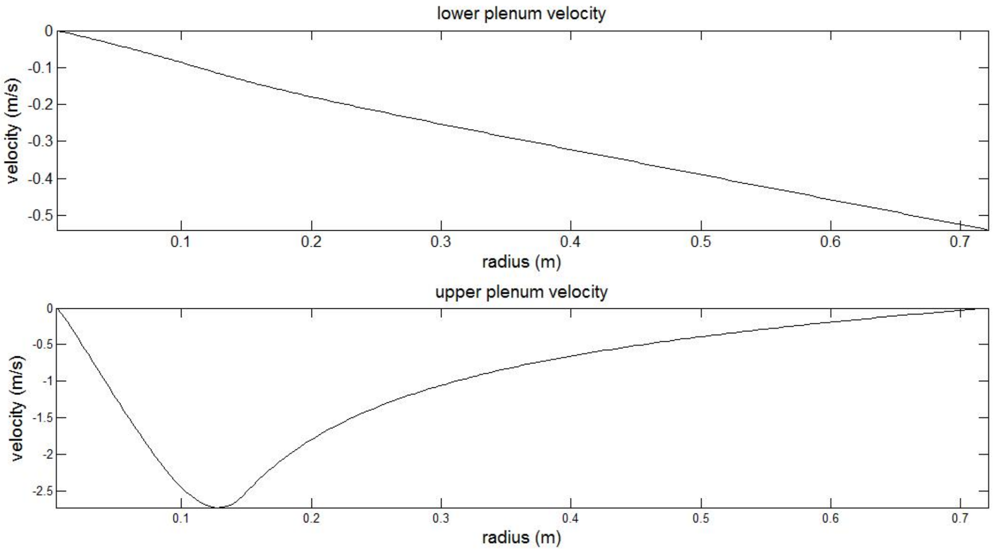

Figure 5.4: Radial velocity profiles in the lower and upper plenum at nominal flow rate.

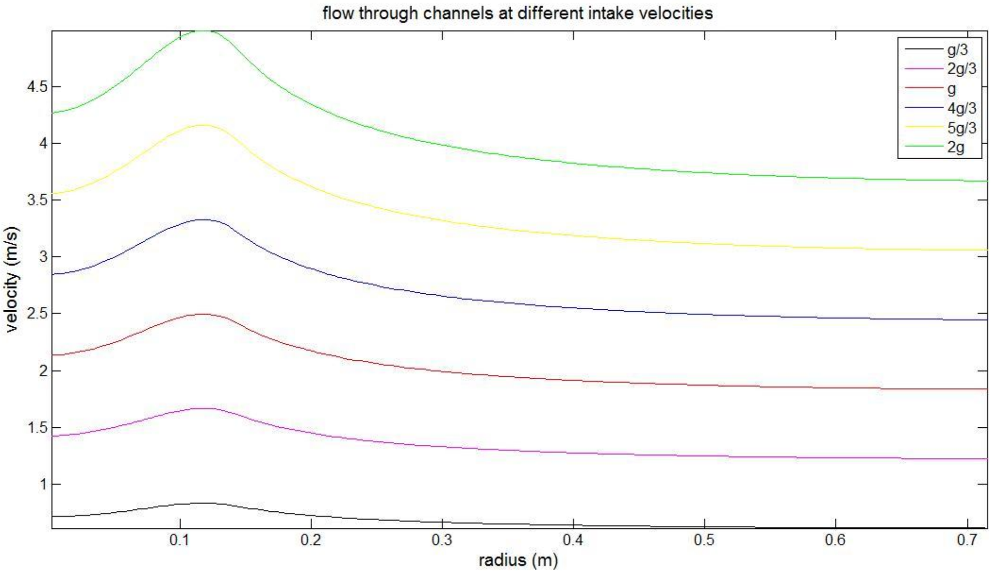

Figure 5.5: Steady state axial velocity profiles for six different flow rates, tabulated in 5.2.

The effect of the pressure regain (γ_l) in the lower plenum due to the discharge of salt can be seen in Fig. 5.3 (1^{st} figure). The pressure gradually builds up when going from the outside, $r = r_{max}$, of zone 1 to the inside at $r = 0$, although the differences are quite small. The pressure differences are somewhat bigger in the upper plenum, Fig. 5.3 (2^{nd} figure). Pressure losses (γ_u) due to the intake of salt from channels are clearly visible up until the point where the outlet header starts. From that point on, salt is removed from the upper plenum and both pressure regain and loss start playing a part.
The average radial velocities $\langle u \rangle$ in the upper and lower plenums are depicted in Fig. 5.4. Since the gradient in the pressure of the lower plenum is fairly constant, the velocity follows suit. The velocity in the upper plenum has to increase because of the intake of salt, up until the point where the outlet header starts.

5.3 Calculations at different flow rates

Computations are performed at different flow rates to see whether and how the steady state axial velocity distribution in the reactor core (zone 2) changes with different intake velocities. The axial velocity profiles are shown in Fig. 5.5. Intake flow rates for which calculations are performed are listed in 5.2.

$$g(t) = \begin{array}{l} g_1 = 1/3 g_{nom} \\ g_2 = 2/3 g_{nom} \\ g_3 = g_{nom} \\ g_4 = 4/3 g_{nom} \\ g_5 = 5/3 g_{nom} \\ g_6 = 2 g_{nom} \end{array} \tag{5.2}$$

Fig. 5.5 shows that the overall shape of the velocity profiles remains the same for different intake flow rates. The highest velocity is still some 30% greater than the lowest velocity for all profiles and as a result, the profiles with higher intake velocities are more pronounced. These results show that increasing the flow rate of the MSR leads to a less uniform velocity distribution which may have an impact on heat exchange properties and the neutron flux profile.

5.4 Start up transient

Since there is no data describing the precise flow rate of salt as a function of time during a start up transient in the MSRE, an estimation about the exact behavior has to be done. For the start up transient an estimation of the flow rate as a function of time was done in [1] by comparing the flow rate of the coolant during

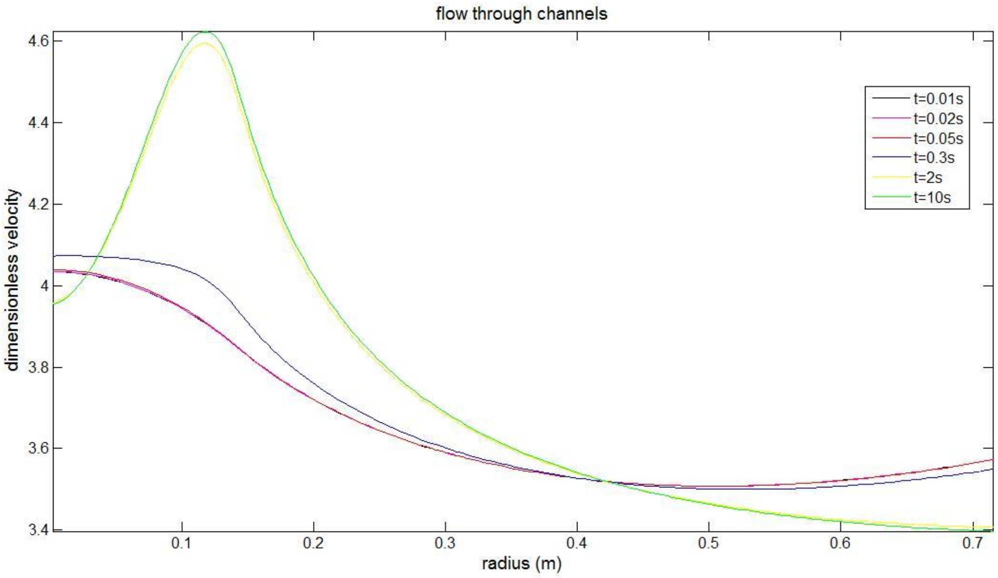

Figure 5.6: Axial velocity field during a start up transient. Velocities are normalized with respect to the intake velocity at that instant in time.

start up with the flow rate of the salt. The following results were obtained:

$$g(t) = \begin{array}{ll} g_{nom}(e^{t\cdot 0.5993} - 1) & t \leq 0.5625 \\ g_{nom}(1 - e^{-(t-0.15625)/0.794}) & 0.5625 < t \leq 10 \\ g_{nom} & t > 10 \end{array} \tag{5.3}$$

From these equations, the velocity at the intake can be used as input as a function of time. The resulting axial velocity distribution in the reactor core (zone 2), normalized with respect to the intake velocity at that instant in time, is plotted in figure Fig. 5.6. Table 5.4 shows the inflow of salt at the six different times for which the axial velocity distribution is plotted.

$$g(t) = \begin{array}{l} g_1(t = 0.01) = 0.006012 g_{nom} \\ g_2(t = 0.02) = 0.01206 g_{nom} \\ g_3(t = 0.05) = 0.03042 g_{nom} \\ g_4(t = 0.3) = 0.1969 g_{nom} \\ g_5(t = 2) = 0.9022 g_{nom} \\ g_6(t = 10) = g_{nom} \end{array} \tag{5.4}$$

Fig. 5.6 shows that it takes at least more than $0.3s$ before the velocity profile resembles the steady state axial velocity profiles calculated in previous sections. Depending on the convergence criterium, it may take as much as $5s$ before 'true' steady state is reached. Since the velocities are normalized with respect to the intake velocity one has to take into account that right after start up, the axial velocities are almost zero and therefore variations will not have a dramatic effect.

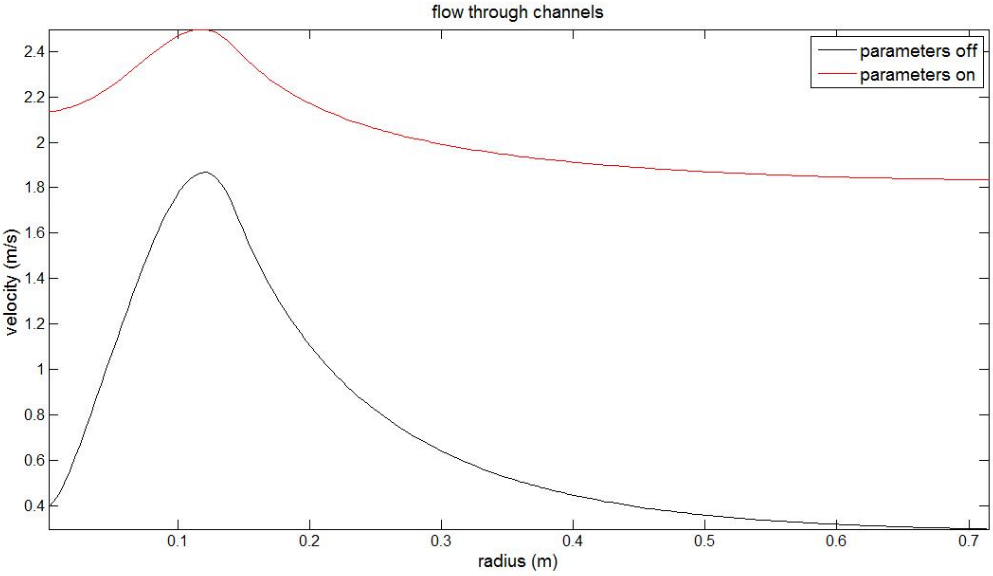

Figure 5.7: Axial velocity field in core of the MSRE at nominal flow with changed parameters. The changes made are summarized in 5.5, thereby neglecting some model assumptions. The scale of the changed axial velocity profile is somewhat different because the porosity no longer has any influence, making the area over which the axial discharge occurs larger and therefore the average axial velocity lower. The original steady state axial velocity profile at nominal flow is plotted red for easy reference. The changed profile is plotted black.

Still, differing profiles during start up will have to be taken into account in further calculations to enhance accuracy.

5.5 Sensitivity of the code to the different model parameters

The development of the model and code involved a lot of modeling and simplifications and it is important to note that these simplification and assumptions about the relevant physical processes go not without consequence. The different parameters like α, β and γ_l, to name a few, all leave their mark on the final solution as provided by the code. Setting these parameters to 1 and thereby neglecting some of the model assumptions results in somewhat different pressure and velocity fields, an example of which is presented in Fig. 5.7, plotted in black, along with the 'original' axial velocity distribution at nominal flow, plotted red. The scale is different because the porosity no longer has any influence, making the area over which the axial discharge occurs larger and therefore the average axial velocity lower. An overview of the changed parameter with respect to table 5.1 is presented in 5.5. Although the effects may be quite severe, the overall

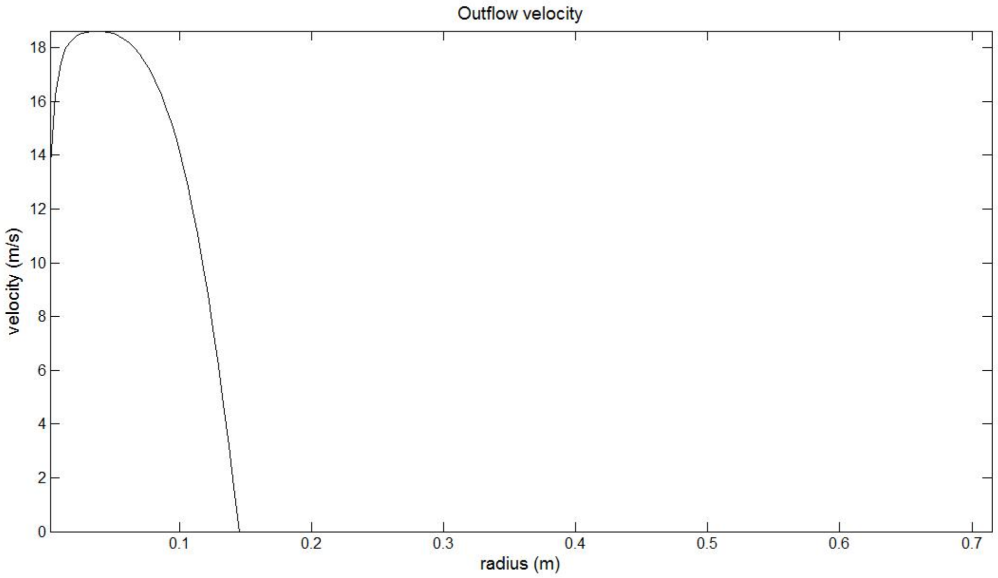

Figure 5.8: Steady state axial velocity field in the outflow header of the MSRE at nominal flow. The gradient in the axial velocity should theoretically tend to zero near $r = 0$, a result which the code is not able to produce.

shape of the solution is clearly retained.

$$\begin{array}{ll} \text{Turning loss} & T_l = 0.0 \\ \text{Porosity} & \lambda = 1.0 \\ \text{Perimeter ratio} & \beta = 1.0m^{-1} \\ \text{Pressure regain} & \gamma_l = 1.0 \\ \text{Pressure loss} & \gamma_u = 1.0 \end{array} \tag{5.5}$$

Omitting the quasi-convective term, in the form of $(1 + T_l)w_i^2$, in the reactor core leads however to an entirely different solution. It also greatly increases convergence time and the time step needs to be reduced significantly. This result was not expected since the true convective term in the axial momentum equation could be easily omitted because of mass conservation, which led to the belief that the quasi-convective term would not be of much influence and that the pressure difference between the two plenums would play the dominant role in establishing the steady state axial velocity field. Apparently, turning losses do have a major influence in the model and code.

5.6 Further problems and general remarks on the validity of the code

Since the outflow is modeled as a simple cylindrical pipe and the salt acts as a viscous fluid one would expect some form of Poiseuille flow [13]. The code is however not able to produce the expected result but rather generates the axial velocity distribution in the outflow depicted in Fig. 5.8. A lot of effort went into finding a solution to this problem; unfortunately without result. Apparently the code and/or model are not able to produce the expected result, since the gradient in the axial velocity should tend to zero when approaching $r = 0$. Although the model assumptions made with regard to the stresses involved in the MSRE system seem to be valid over a wide range of Reynolds numbers according to [2] on who's work a large part of the model presented here is based, it remains hard to verify if the code truly gives an accurate representation of reality. Other than the benchmark checks performed in 4 and critical review of the results the code produces there is little possibility of further validation of the model and code because no experimental data is available. However, studies done on theoretical MSR designs other then the MSRE setup investigated here, like [14] [7] give reason for optimism. In these studies, a different approach to model the axial velocity distribution is presented and the geometry of the reactor vessel is somewhat different so it is hard to do a direct comparison but at least in shape the axial velocity distributions look similar. Both approaches predict an increase in velocity when going from the outside $r = r_max$ to the inside $r = 0$ of the reactor core (zone 2).

Chapter 6

Conclusions and recommendations

The model and code developed in this thesis serve to provide pressure and velocity distributions in the reactor vessel of a molten salt reactor. At a given flow rate computations may be done, the results of which can be used as input for further studies into the behavior of a molten salt reactor. The axial velocity distribution in the reactor core is of special interest since most studies on the molten salt reactor done so far only take into account a single axial velocity for the entire core structure and therefore do not provide insight into how convective transport of precursors as a function of the radius might influence the flux profile of a molten salt reactor or how a non-uniform distribution might influence heat exchange properties.

Computations performed in this study show that the axial velocities in the channels of the reactor core of the MSRE setup may vary as much as 30% at nominal flow, a result which shows that using a single axial velocity for the entire core is a rather crude estimate. Also, during start up, the shape of the axial velocity profile may vary with time and increasing the flow rate at the intake leads to a higher variation of velocities in the profile. These results will need to be taken into account in future neutronics or thermal-hydraulics calculations.

Because of the complex geometry of the MSRE, a lot of assumptions had to be made about the physical transport phenomena taking place in the reactor core. Although the benchmark checks from 4 give reason for optimism, there still remain issues for which there is no direct and simple answer. Studies on a different, and theoretical type of MSR like [14] produce axial velocity distributions of a similar shape as the distributions presented here. These designs however contain no outflow like the MSRE. Modeling of the outflow seems to cause problems because of the non-zero outflow velocity gradient and may require further attention in future studies.

In order to gain further detailed insight into velocity and pressure fields, and maybe simulate the blockage of a single channel (which this code isn't able to do), a more elaborate model in three dimensions would have to be developed. This would however soon become very involved and the computational cost would become tremendous.

All in all, the code and model presented in this thesis seem capable of producing detailed and viable results which may be used to gain further insight into the behavior of molten salt reactors. Apart from the MSRE, a benchmark for most calculations, other theoretical designs may be studied using the code presented here by simply altering geometrical values and other relevant parameters. The code is able to simulate transients by supplying the intake flow rate as a function of time. Convergence time is short and computational effort is low which were key requirements for the code to be integrated in future, more elaborate coupled thermal-hydraulics and neutronics calculations that will deepen the understanding of the fascinating Molten Salt Reactor.

Bibliography

[1] G. J. Auwerda. *Computational modeling of a molten salt reactor.* RID, 2007. [cited at p. 3, 39]

[2] R. A. Bajura. A model for flow distribution manifolds. *Journal for engineering power*, 1971. [cited at p. 7, 12, 20, 43]

[3] J.G.M. Eggels. *Direct an large eddy simulation of turbulent flow in a cylindrical pipe geometry.* Delft University Press, 1994. [cited at p. 8, 29]

[4] J. Kophazi D. Lathouwers J. Kloosterman S. Feher. Three-dimensional space and time-dependent analysis of molten salt reactors. 2003. [cited at p. 3]

[5] A. L. Garcia. *Numerical methods for physics.* Prentice Hall, 2000. [cited at p. 15, 16, 23]

[6] J. J. Dunderstadt L. J. Hamilton. *Nuclear reactor analysis.* Wiley and Sons, 1976. [cited at p. 2]

[7] T. Yamamoto K. Mitachi T. Suzuki K. Ikeuchi. Transient characteristics of small molten salt reactor during blockage accident. 2006. [cited at p. 43]

[8] K. Hanjalic S. Kenjeres M. J. Tummers H. J. J. Jonker. *Advanced Physical Transport Phenomena.* Delft University Press, 2003. [cited at p. 15, 16, 22, 24]

[9] R. A. Bajura E. H. Jones JR. Flow distribution manifolds. *Transactions of the ASME*, 1976. [cited at p. 7, 10, 13, 20, 29, 31, 32]

[10] MOST. *Review of molten salt reactor technology.* 5th Euratom framework programme, 2001. [cited at p. ii, 2, 3]

[11] S. V. Patankar. *Numerical heat transfer and fluid flow.* Taylor and Francis, 1980. [cited at p. 16, 22, 24, 26]

[12] M. J. B. M. Pourquie. *Large eddy simulation of turbulent jet.* Delft University Press, 1994. [cited at p. 8, 18, 22, 24]

[13] Bird Stewart and Lightfoot. *Physical Transport Phenomena.* bla, 2004. [cited at p. 8, 42]

[14] T. Yamamoto K. Mitachi T. Suzuki. Steady state analysis of small molten salt reactor. 2005. [cited at p. 43, 45]

[15] H. v.d. Akker R. F. Mudde. *Physische Transportverschijnselen.* VSSD, 2005. [cited at p. 10, 11]